

A Superconducting Qubit-Resonator Quantum Processor with Effective All-to-All Connectivity

Michael Renger,^{1,*} Jeroen Verjauw,^{1,*} Nicola Wurz,^{1,*} Amin Hosseinkhani,¹ Caspar Ockeloen-Korppi,² Wei Liu,² Aniket Rath,¹ Manish J. Thapa,¹ Florian Vigneau,¹ Elisabeth Wybo,¹ Ville Bergholm,² Chun Fai Chan,² Bálint Csátári,² Saga Dahl,² Rakhim Davletkaliyev,² Rakshyakar Giri,¹ Daria Gusenkova,¹ Hermanni Heimonen,² Tuukka Hiltunen,² Hao Hsu,¹ Eric Hyypä,² Joni Ikonen,² Tyler Jones,¹ Shabeeb Khalid,² Seung-Goo Kim,² Miikka Koistinen,² Anton Komlev,² Janne Kotilahti,² Vladimir Kukushkin,² Julia Lamprich,¹ Alessandro Landra,² Lan-Hsuan Lee,² Tianyi Li,² Per Liebermann,² Sourav Majumder,¹ Janne Mäntylä,² Fabian Marxer,² Arianne Meijer - van de Griend,² Vladimir Milchakov,² Jakub Mrožek,² Jayshankar Nath,¹ Tuure Orell,² Miha Papič,^{1,3} Matti Partanen,² Alexander Plyushch,² Stefan Pogorzalek,¹ Jussi Ritvas,² Pedro Figuero Romero,¹ Ville Sampo,² Marko Seppälä,² Ville Selinmaa,² Linus Sundström,² Ivan Takmakov,² Brian Tarasinski,² Jani Tuorila,² Olli Tyrkkö,² Alpo Välimaa,² Jaap Wesdorp,² Ping Yang,¹ Liuqi Yu,² Johannes Heinsoo,² Antti Vepsäläinen,² William Kindel,¹ Hsiang-Sheng Ku,¹ and Frank Deppe^{1,†}

¹*IQM Quantum Computers, Georg-Brauchle-Ring 23-25, 80992 Munich, Germany*

²*IQM Quantum Computers, Keilaranta 19, 02150 Espoo, Finland*

³*Department of Physics and Arnold Sommerfeld Center for Theoretical Physics, Ludwig-Maximilians-Universität München, Theresienstr. 37, 80333 Munich, Germany*

(Dated: March 17, 2025)

In this work we introduce a superconducting quantum processor architecture that uses a transmission-line resonator to implement effective all-to-all connectivity between six transmon qubits. This architecture can be used as a test-bed for algorithms that benefit from high connectivity. We show that the central resonator can be used as a computational element, which offers the flexibility to encode a qubit for quantum computation or to utilize its bosonic modes which further enables quantum simulation of bosonic systems. To operate the quantum processing unit (QPU), we develop and benchmark the qubit-resonator conditional Z gate and the qubit-resonator MOVE operation. The latter allows for transferring a quantum state between one of the peripheral qubits and the computational resonator. We benchmark the QPU performance and achieve a genuinely multi-qubit entangled Greenberger-Horne-Zeilinger (GHZ) state over all six qubits with a readout-error mitigated fidelity of $F_{|\psi\rangle_{\text{GHZ}}} = 0.86$.

I. INTRODUCTION

The design flexibility of superconducting qubits facilitates the exploration of innovative quantum processing architectures with different topologies. Currently, quantum processors built from regular lattices of sparsely connected superconducting qubits have been at the center of the effort in scaling superconducting quantum processing units (QPUs) by major industrial and governmental players, with example topologies including square lattice [1, 2], heavy hex [3] and square-octagon [4]. In these topologies, each of the qubits is connected to at most four neighboring qubits. These QPUs are conceptually straightforward to scale, suited for applications such as the square lattice surface code [5, 6], and have achieved breakthroughs in science and engineering including the simulation of a Bose-Hubbard lattice [7] and trotterized Ising model [8], as well as lattice surgery [9]. However, achieving quantum utility remains elusive [10–13]. Many applications on these QPUs require additional gates, or

SWAP networks, because the connectivity of the QPU in terms of native two-qubit gates is not matched to the application, thereby reducing the circuit fidelity [14]. Moreover, the connectivity of these QPUs is not well-suited to efficiently execute quantum error correcting codes with high encoding rates [15].

Alternative quantum processor architectures [16], relying on central nodes offer freedom for customizing connectivity [17, 18]. A promising choice for this central node is a resonator which has a long history in circuit QED [19, 20]. Such architectures, consisting of qubits coupled to a bus resonator, have demonstrated genuine multipartite entangled states for up to 20 qubits [21, 22]. They provide the flexibility to design the connectivity of a quantum processor and thus to adapt it to the desired application, including noisy intermediate scale quantum (NISQ) algorithms [14, 23] and error correction codes. Furthermore, they allow for combining conventional qubit-based quantum computing with bosonic resonator modes that provide additional computational degrees of freedom [24–28]. Such quantum computing modality combines the precise control of qubits with the large Hilbert space of bosonic modes. Realizing QPUs with these architectures requires engineering and mastering the control of qubit-resonator interactions and developing new methods for benchmarking.

* M. R., J. V. and N. W. contributed equally;
michael.renger@meetiqm.com, jeroen.verjauw@meetiqm.com,
nicola.wurz@meetiqm.com

† frank.deppe@meetiqm.com

In this paper we introduce a qubit-resonator QPU where a computational resonator is connected to six peripheral qubits in a star topology with frequency-tunable couplers. These couplers allow for addressing individual qubit-resonator pairs while simultaneously suppressing the hybridization cross-talk to the spectator qubits. We implement and benchmark two qubit-resonator operations, which combined with single-qubit gates, form a universal set of quantum operations for this QPU. The qubit-resonator operations are based on the Jaynes-Cummings interaction between a qubit and the central computational resonator (CR) [20]. For the MOVE operation we restrict the input state of the qubit-resonator pair to the single-photon manifold and tune the qubit and the resonator into resonance in order to fully transfer a state between them. In addition, we implement a conditional Z (CZ) gate to create entanglement between a qubit and the resonator. The CZ gate is implemented by tuning the e-f transition of the qubit into resonance with the computational resonator [29]. After a full Rabi cycle, the state where both the qubit and the computational resonator are in the first excited state has acquired a π phase shift. By combining these qubit-resonator operations, we can effectively implement a CZ gate between any two qubits. We consider our system as a QPU with effective all-to-all connectivity between the qubits, because a constant overhead of two MOVE operations is required to realize a qubit-qubit CZ gate - independent of the physical distance between the qubits. Depending on the algorithm, however, it may be beneficial to treat the resonator as a proper computational element by applying MOVE and CZ operations individually. As an example for such an algorithm and to provide a global benchmark for the quantum computing capability of our QPU, we entangle all qubits in a Greenberger-Horne-Zeilinger (GHZ) state. As an outlook towards hybrid quantum computing including higher order Fock states, we demonstrate that the higher resonator levels can be populated by repeatedly exciting the qubit and applying the MOVE operation. We eventually provide a NISQ application use case for our QPU by applying error mitigation to determine the ground state energy of the transverse-field Ising model.

II. QUBIT-RESONATOR QPU

The QPU consists of six frequency-tunable superconducting transmon qubits (QB) [30], connected to a central computational resonator in a star topology, see Fig. 1(a). The central resonator is implemented by a coplanar waveguide transmission line in the quarter wavelength configuration. To achieve tunable coupling with a large on-off ratio, we employ an additional frequency-tunable transmon qubit as coupling element [29, 31] between the resonator and each qubit. Analog to their use in qubit-qubit gates, these tunable couplers (TCs) mediate an effective qubit-resonator interaction, by creating

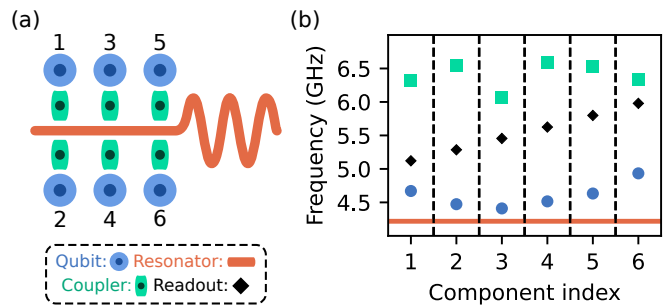


FIG. 1. (a) Schematic illustration of the qubit-resonator QPU. The readout resonators (one for each qubit) have been omitted for the sake of clarity. (b) Frequencies of the qubits (blue circles), the tunable couplers (green squares), the computational resonator (red line), and the dispersively coupled resonators used for multiplexed readout (black diamonds). The qubit and coupler frequencies correspond to their first-order flux insensitive configuration.

an indirect coupling with a tunable sign and magnitude in addition to a small fixed qubit-resonator coupling. During gate operation, the couplers are dynamically tuned near the qubit and computational resonator frequencies, enabling fast non-adiabatic gate operation. On the other hand, in the idling configuration the total ZZ -coupling can be suppressed to a very small value on the order of a few kilohertz by choosing the tunable coupler frequency such that the coupler-mediated and direct couplings cancel each other. The frequencies of all the QPU components are shown in Fig. 1(b).

To maximize the coupling strengths, we connect the tunable couplers to the open-circuit end of the resonator. To enable flexible positioning of the qubits with respect to the computational resonator, we employ coupler extender waveguides between the components and the coupler [31]. We note that the star topology with a computational resonator as the central element can be extended beyond the six peripheral qubits shown here without fundamental limitations. We estimate that, using similar coupling values as reported here and maintaining the mm-scale spacing between neighboring qubits, up to twelve qubits can be coupled to such a single computational resonator. The qubit-resonator QPU design methodology is discussed in Appendix B.

The QPU further contains drive lines for XY -control of the qubits, flux bias lines to control the qubit and tunable coupler frequencies, and readout resonators that enable multiplexed dispersive readout of the qubit state. The design of the control lines and readout structures closely follows the design in Ref. [31].

III. QUBIT-RESONATOR OPERATIONS AND CHARACTERIZATION

We achieve effective all-to-all connectivity on the qubit-resonator QPU with star topology by implement-

ing CZ gates between each pair of qubits. To realize a CZ gate CZ(QB2, QB1) between a pair of qubits, QB1 and QB2, we transfer the state from one of the qubits, i.e., QB1 to the computational resonator by applying MOVE(QB1, CR). Consecutively, we perform a CZ(QB2, CR) gate between the CZ qubit, QB2, and the resonator to entangle the two components. Then, as the last step, we apply a second MOVE operation MOVE(QB1, CR), which transfers the entanglement with QB2 from the computational resonator to the MOVE qubit, QB1. Hence, to create entanglement between the peripheral qubits of the device, both native qubit-resonator operations are required, the MOVE operation and the CZ gate.

The MOVE operation transfers a state from a qubit to the computational resonator or vice versa, assuming that only one of the two components is populated beforehand. We implement this operation using the resonant Jaynes-Cummings interaction described by the Hamiltonian:

$$\hat{H}_{\text{JC}} = \frac{\hbar\omega_{\text{QB}}}{2}\hat{\sigma}_z + \hbar\omega_{\text{CR}}\left(\hat{a}^\dagger\hat{a} + \frac{1}{2}\right) + \frac{\hbar\Omega}{2}(\hat{a}\hat{\sigma}^+ + \hat{a}^\dagger\hat{\sigma}^-), \quad (1)$$

where \hat{a} (\hat{a}^\dagger) is the annihilation (creation) operator for the computational resonator mode, $\hat{\sigma}^+ \equiv |e\rangle\langle g| = (\hat{\sigma}^-)^\dagger$ are the raising and lowering operators for the qubit, and Ω is the Rabi rate. For the MOVE operation, the qubit frequency, ω_{QB} , is adjusted to match the computational resonator frequency, ω_{CR} . We experimentally realize this operation by applying a magnetic flux pulse on the qubit SQUID loop.

In general, the Jaynes-Cummings interaction couples a qubit with the entire ladder of resonator number states. By integrating the time evolution of the Jaynes-Cummings interaction given in Eq. (1) for a fixed duration, we derive the unitary of the Jaynes-Cummings gate given by the transformation of the basis states

$$\begin{aligned} |g, n\rangle &\rightarrow c_n(\Theta)|g, n\rangle - is_n(\Theta)|e, n-1\rangle, \\ |e, n\rangle &\rightarrow c_{n+1}(\Theta)|e, n\rangle - is_{n+1}(\Theta)|g, n+1\rangle, \end{aligned} \quad (2)$$

where we define

$$c_n(\Theta) \equiv \cos\left(\frac{\sqrt{n}\Theta}{2}\right), \quad s_n(\Theta) \equiv \sin\left(\frac{\sqrt{n}\Theta}{2}\right). \quad (3)$$

Here, the angle $\frac{\Theta}{2} = \frac{1}{2}\int\Omega(t)dt$ is the exchange angle that parametrizes the Jaynes-Cummings gate. The MOVE operation, defined for the input states $|g, 1\rangle$, $|e, 0\rangle$ and $|g, 0\rangle$ is calibrated to achieve a full population exchange of $|g, 1\rangle$ and $|e, 0\rangle$, corresponding to an exchange angle of $\Theta = \pi$. In this case, we use the abbreviations $c_n \equiv c_n(\pi)$, $s_n \equiv s_n(\pi)$.

For conventional quantum computing applications, we restrict the resonator such that it is never occupied beyond the first excited state, and thus it can be effectively

mapped onto the state space of a qubit. Specifically, we carefully design the gate sequences so that the MOVE operation is never applied to a qubit-resonator state with an $|e, 1\rangle$ contribution. As can be seen from the description of the Jaynes-Cummings gate in Eq. (2), the system evolves into the state $c_2|e, 1\rangle - is_2|g, 2\rangle$ if the MOVE operation is applied to $|e, 1\rangle$, thereby breaking the qubit mapping of the resonator by occupying its $|2\rangle$ state.

By avoiding the $|e, 1\rangle$ state when applying the MOVE operation, we can operate within the single photon manifold where we can conceptually treat the resonator as a qubit. By subsequently removing the restrictions on the resonator, we can access higher resonator modes.

A. QPU Characterization

To perform quantum operations on the qubit-resonator QPU, we employ six microwave drive lines for XY-control of the qubits and twelve flux lines to enable frequency tuning of the qubits and the tunable couplers with Z pulses. Details of the experimental setup can be found in Appendix A. We determine the qubit frequencies from a variable delay Ramsey experiment and extract the qubit and coupler flux dispersion by sweeping the applied DC bias. We implement single-qubit gates using the derivative removal by adiabatic gate (DRAG) method with a cosine shaped envelope of the in-phase component [32]. We employ error amplification techniques to reach an average individual single-qubit gate fidelity of $99.94 \pm 0.09\%$ [33]. We characterize the coherence times of all qubits in their first-order flux-insensitive configuration. We calculate the average energy relaxation time $T_1 = 41.3 \pm 1.3 \mu\text{s}$, i.e., the arithmetic mean over all qubits. Using a Ramsey sequence, we find an average dephasing time of $T_2^* = 33.0 \pm 1.2 \mu\text{s}$. To remove the effect of quasi-static noise, we perform a Hahn echo experiment and obtain an average echo dephasing time of $T_2^e = 45.8 \pm 1.2 \mu\text{s}$. We find an exponential decay envelope, implying white noise as dominating source of decoherence [34, 35].

Since the computational resonator state cannot be directly prepared and read out, we measure its coherence properties indirectly by transferring a state between one of the qubits and the resonator using the MOVE operation. For the resonator relaxation time, we obtain $T_1 = 5.53 \pm 0.32 \mu\text{s}$. Via a Ramsey sequence, we measure a resonator dephasing time of $T_2^* = 10.9 \pm 1.0 \mu\text{s}$ close to $2T_1$, implying that the resonator coherence is limited by energy relaxation. We furthermore extract the computational resonator frequency at the idling configuration, $\omega_{\text{CR}} = 4.218 \text{ GHz}$. Details about the measurement techniques for the resonator parameters are given in Appendix E3 and a summary of the QPU parameters can be found in Appendix E.

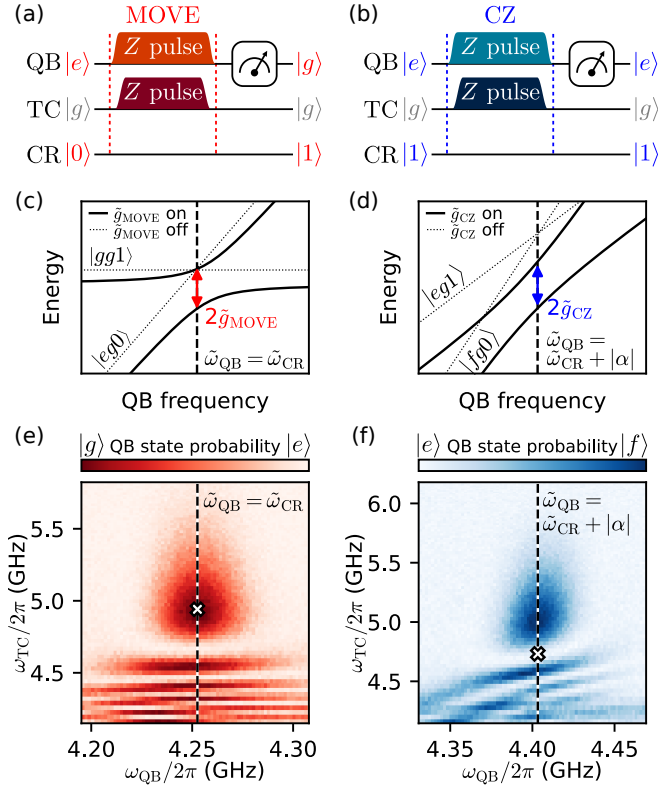


FIG. 2. Qubit-resonator gate calibration. (a), (b) Pulse level schedules used for tuning up the population exchange of the MOVE operation and the CZ gate, respectively. For the MOVE operation, initially only the qubit is in the excited state, while for the CZ gate both the qubit and the computational resonator start in the first excited state. (c), (d) Energy level diagrams showing the relevant states involved in the MOVE operation and the CZ gate, respectively. Both diagrams depict the diabatic (dotted grey line) and dressed (black solid line) energy levels. The energy splittings ($2\tilde{g}_{\text{MOVE}}$, $2\tilde{g}_{\text{CZ}}$) are tuned by adjusting the coupler frequency ω_{TC} . (e), (f) Population oscillations (the energy levels shown in (c) and (d), respectively, are obtained by scanning the qubit frequency during the gate, ω_{QB} , over the resonance condition (indicated by the black dashed line), and by tuning the effective interaction strength between the qubit and the computational resonator during the gate by adjusting the coupler frequency, ω_{TC} . The white crosses indicate the initial guesses for the operating point of the gates based on the population oscillations.

B. Calibration of Qubit-Resonator Gates

In the following, we discuss the calibration of the qubit-resonator MOVE operation and the qubit-resonator CZ gate.

We use the notation $|\text{QB}, \text{TC}, \text{CR}\rangle$ to represent the eigenstates of the system (with $|g\rangle$, $|e\rangle$, $|f\rangle$ for qubit and coupler eigenstates, and $|0\rangle$, $|1\rangle$ as resonator number states), which approximate the diabatic eigenstates of the system, i.e., at the idling configuration. The idling configuration is a chosen set of qubit, coupler and res-

onator frequencies which results in a minimal residual ZZ-interaction. We implement the qubit-resonator gates using non-adiabatic transitions between $|eg0\rangle$ and $|gg1\rangle$ for the MOVE operation, and $|eg1\rangle$ and $|fg0\rangle$ for the CZ gate, see Fig. 2(a) and Fig. 2(b). This population exchange is initiated by first bringing the involved qubit-resonator states into resonance and then quickly tuning the frequency of the coupler to increase the interaction strength \tilde{g}_{MOVE} between $|eg0\rangle$ and $|gg1\rangle$, or \tilde{g}_{CZ} between $|eg1\rangle$ and $|fg0\rangle$, respectively. As shown in Fig. 2(c) and Fig. 2(d), the interaction between the involved qubit-resonator states opens up an avoided crossing with an energy gap of $2\tilde{g}_{\text{MOVE}}$ or $2\tilde{g}_{\text{CZ}}$, respectively, and shifts the energy levels downwards due to the dispersive interaction with the coupler. For the MOVE operation, the eigenenergies of the dressed states fulfill $\tilde{\omega}_{\text{QB}} = \tilde{\omega}_{\text{CR}}$. This resonance condition differs from the bare frequencies and is the result of different hybridizations between the qubit, coupler and resonator as illustrated in Appendix D. The operating point of the MOVE operation is determined from a measurement of the population exchange as shown in Figure 2(e). For the CZ gate, we tune the $|eg1\rangle$ and $|fg0\rangle$ states close to resonance such that $\tilde{\omega}_{\text{QB}} = \tilde{\omega}_{\text{CR}} + |\alpha|$. Here α is the anharmonicity of the qubit participating in the CZ gate. Similarly to the MOVE, we measure the population exchange of the CZ qubit as shown in Figure 2(f). In contrast to above, however, the operating point of the CZ gate is where the qubit, starting in $|e\rangle$, completes a *full* oscillation through $|f\rangle$ and returns back to the initial $|e\rangle$ state, as the CZ gate only modifies the phase and not the population of the basis states. The full tune-up procedure for both qubit-resonator gates, including the calibration of the conditional π phase shift required for the CZ gate, is discussed in detail in Appendix E. A derivation of the analytical expression for the conditional phase is presented in Appendix D.

During the qubit-resonator gates, the transition frequencies of both components change, resulting in the accumulation of single-qubit phases. We correct for these phases by applying virtual Z (VZ) gates to the respective XY qubit drive pulses [36]. To obtain the optimal VZ correction for the qubit when applying the MOVE operation, we perform the operation an even number of times and calibrate the common phase obtained when moving a superposition state from the qubit to the computational resonator and back. For the CZ gate, two separate VZ corrections are calibrated, one for the computational resonator and one for the CZ qubit. The VZ correction of the computational resonator is determined indirectly via the qubit that was used to prepare the state in the resonator (MOVE qubit). The relative phase rotation of a state that has been transferred to the computational resonator with respect to the rotating frame of the MOVE qubit results in a time-dependent phase that accumulates at a rate corresponding to the frequency difference between the MOVE qubit and the resonator [37]. To properly correct for single-qubit phase accumulation in

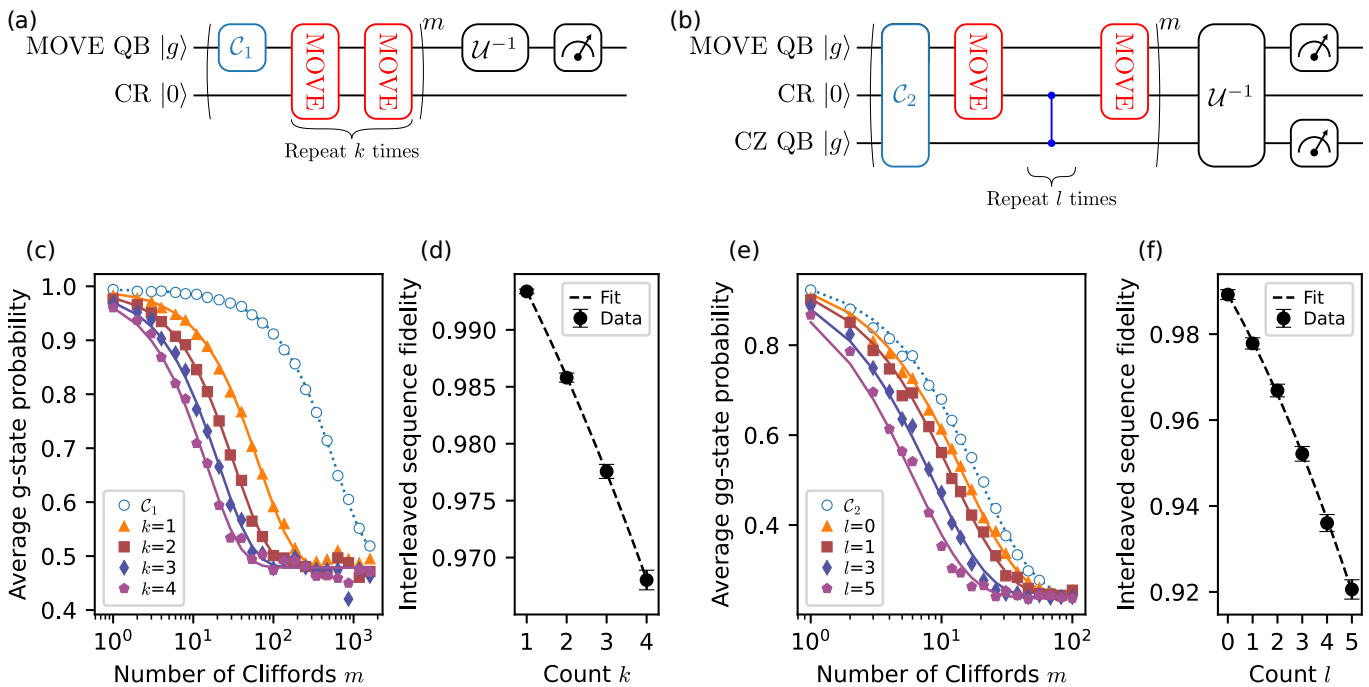


FIG. 3. Interleaved randomized benchmarking experiments for qubit-resonator gates. (a) Circuit for benchmarking the MOVE operation via interleaved randomized benchmarking. The sequence consists of m single-qubit Clifford gates C_1 interleaved with k repetitions of two subsequent MOVE operations, which effectively implement an identity. The final operation U^{-1} inverts the applied sequence. (b) Circuit for benchmarking the CZ gate via interleaved randomized benchmarking. Two-qubit Clifford gates C_2 are interleaved with MOVE-ICZ-MOVE operations for a varying number of CZ gates l . (c) Experimental data of the sequence fidelity for randomized benchmarking with $k = 1, \dots, 4$ interleaved double MOVE operations and the reference single-qubit Clifford sequence (open blue circles) as a function of the number of Clifford gates. (d) Extracted fidelity of the interleaved gate sequence as a function of k (solid black circles) and quadratic fit (dashed line). (e) Experimental data of the sequence fidelity for randomized benchmarking with interleaved MOVE-ICZ-MOVE gate sequences and the reference two-qubit Clifford sequence (open blue circles) as a function of the number of Clifford gates. (f) Extracted fidelity of the interleaved MOVE-ICZ-MOVE gate sequence as a function of l (solid black circles) and quadratic fit (dashed line).

arbitrary algorithms, we need to distinguish this time-dependent phase from fixed phase corrections that depend only on the flux pulse shape implementing a certain gate. Details on the calibration of the single-qubit phase corrections can be found in Appendix E 1 and Appendix E 2.

C. Benchmarking Qubit-Resonator Gates

For benchmarking qubit-resonator gates, we employ the technique of interleaved randomized benchmarking (iRB) [38, 39]. The average gate fidelity is estimated from the decay of the measured qubit population as a function of the applied sequence length m . The iRB circuit for the MOVE operation is shown in Fig. 3(a). Since we apply the MOVE operation only to states for which either the qubit or the computational resonator are unpopulated, the problem of calculating the average gate fidelity reduces from an integration over all possible input states for a bipartite quantum system to considering only a single effective two-level system. Consequently, we benchmark the MOVE operation in the framework of

single-qubit RB interleaving pairs of MOVE operations, which effectively implement an identity gate. To reduce the uncertainty of the extracted double MOVE fidelity, we perform multiple instances of the iRB experiment, interleaving the effective identity gate $(\text{MOVE})^{2k}$ for different integer numbers k . The ground state probability of the qubit is then fitted by $P_k(m) = Ap_k^m + B$, where the depolarization probability p_k is treated as independent fit parameter for each k , and the amplitude A as well as the offset B are fitted simultaneously for all k . For each dedicated m in the iRB experiment, we apply 60 different random Clifford sequences and average the experiment over 256 repetitions. In Fig. 3(c), we show the result of such an iRB experiment for QB 2 for up to $k = 4$. We extract the fidelity per interleaved gate sequence as a function of k , as shown in Fig. 3(d). We observe that the interleaved fidelity can be approximated by the fitting function $f_m(k) = 1 - \alpha_m k^2 - \beta_m k$ [40], where the quadratic contribution results from quasi-static noise and remaining gate calibration errors, and the linear term corresponds to depolarization errors. For example, a small error in the exchange angle of the MOVE operation would subsequently lead to populating higher resonator

modes with increasing k , according to Eq. (2), and the loss in qubit population is, to first order, proportional to k^2 . From the fit, we obtain $\alpha_m = 4.6 \times 10^{-4}$ and $\beta_m = 6.1 \times 10^{-3}$. We determine the fidelity of the double MOVE operation as $F_m = f_m(1) = 99.34 \pm 0.03$. The single-qubit Clifford fidelity, averaged over all six qubits, is 0.9990 ± 0.0002 and the double MOVE fidelity averaged over all qubit-resonator pairs, is $\bar{F}_m = 0.988 \pm 0.006$, where the error bars represent the standard deviation of the respective individual fidelities.

Figure 3 (b) shows the iRB circuit for estimating the qubit-resonator CZ gate fidelity. In order to sample all possible input states for the CZ gate acting between a qubit and a computational resonator, we use the MOVE operation to populate the resonator with an arbitrary state. After applying the CZ gate, the resonator has to be brought back to its vacuum state by applying another MOVE operation. In contrast to the benchmarking of the MOVE operation, here we can use two-qubit Clifford benchmarking and integrate over all possible two-qubit states of the MOVE and CZ qubit. We generate two-qubit Clifford gates from single-qubit gates and effective CZ gates acting between the MOVE and the CZ qubit, which are composed of the native qubit-resonator MOVE and CZ operations. Similar as in iterative iRB [41], we vary the number l of interleaved CZ gates between the two MOVE operations and refer to this experiment as MOVE-ICZ-MOVE iRB. In Fig. 3(e) we show the corresponding iRB result when using QB 1 as the CZ qubit and QB 2 as the MOVE qubit, for up to $l = 5$ CZ gates. We extract the interleaved fidelity as a function of l as shown in Fig. 3(f). The data is obtained using 30 different random Clifford sequences and averaged over 256 repetitions. The interleaved fidelity follows $f_{cz}(l) = \gamma_m - \alpha_{cz}l^2 - \beta_{cz}l$, in analogy to $f_m(k)$. Here, the offset γ_m quantifies the errors induced by the MOVE operation at the beginning and at the end of the interleaved sequence. We note that the data point at $l = 0$ follows the quadratic trend for $l \geq 1$, therefore we can assign individual errors to the MOVE and CZ operations, even though they do not commute. From the quadratic fit shown in Fig. 3(f), we obtain $\alpha_{cz} = 7.32 \times 10^{-4}$, $\beta_{cz} = 1.01 \times 10^{-2}$ and $\gamma_m = 0.989$. We observe that γ_m is slightly smaller than the double MOVE fidelity, F_m , extracted from the single-qubit RB presented above. We attribute the mismatch in the fidelity to the idling infidelity of the CZ qubit during the two MOVE operations, which only affects γ_m . Furthermore, the input state sampling in two-qubit Clifford benchmarking is different as compared to single-qubit RB, which can slightly affect the inferred double MOVE fidelity. We extract the fidelity of an individual CZ gate between QB 1 and the computational resonator as $F_{cz} = f_{cz}(1)/\gamma_m = 98.90 \pm 0.05$. Because the value of the quadratic coefficient, α_{cz} , is small compared to the linear coefficient, β_{cz} , we conclude that the depolarization error is the main mechanism limiting the CZ gate fidelity. The corresponding two-qubit Clifford fidelity is 0.9625 ± 0.0007 . Furthermore, we average the

fidelity of all six qubit-resonator CZ gates and obtain $\bar{F}_{cz} = 0.983 \pm 0.009$, where the error bar represents the standard deviation over the respective individual gate fidelities. The individual double MOVE and CZ fidelities are listed in Appendix E.

Next, we estimate the fidelity limits set by decoherence [42]. For the CZ gate, we additionally take into account that we leave the computational space during the $|1, e\rangle \leftrightarrow |2, g\rangle$ population exchange cycle [43]. Details about the coherence limit estimation are provided in Appendix F. An estimate for the coherence limit averaged over all qubit-resonator pairs is $\bar{F}_m^c = 0.993 \pm 0.001$ for the double MOVE operation, and $\bar{F}_{cz}^c = 0.993 \pm 0.002$ for the CZ gate. These values provide an upper bound for the coherence-limited fidelity because the coherence times used in the calculation are measured at the qubit idling frequency configuration, while there is increased flux sensitivity due to qubit frequency tuning during the gate operation. In addition, we do not take hybridization with the coupler into account. Consequently, at least 58.3% (41.2%) of the double MOVE (CZ) infidelity are attributed to decoherence during the operation.

IV. QUBIT-RESONATOR QPU APPLICATIONS

We demonstrate the capabilities of our qubit-resonator QPU and inspire further algorithmic development by presenting four distinct examples. First, we investigate the generation of multipartite entanglement by preparing GHZ states. Next, we use the Q-score benchmark to determine the ability of our QPU to solve combinatorial optimization problems. Finally, we discuss how the MOVE operation can be used as a true Jaynes-Cummings gate to access the higher levels of the computational resonator and present a simulation of the ground state energy of the transverse field Ising model using a variational approach.

A. GHZ State Preparation

As a global benchmark for the QPU performance, we examine its quantum entanglement properties. A fundamental criterion for quantum computing is the ability to entangle all qubits in the processor into a genuinely multi-qubit entangled (GME) state. Here we demonstrate GME by preparing an n -qubit GHZ state [44], which is defined as $|\psi\rangle_{\text{GHZ}} = \frac{|g\rangle^{\otimes n} + |e\rangle^{\otimes n}}{\sqrt{2}}$. We generate the GHZ state by employing two MOVE operations between a single qubit and the computational resonator and an interleaved cascade of qubit-resonator CZ gates, see Fig. 4 (a). In between, multiple CZ gates are applied to entangle the computational resonator with all the peripheral qubits (apart from the MOVE qubit). Therefore, the only overhead in the number of gates as compared to the case of a square grid topology, are the two MOVE operations, which are required to (de)populate the computational resonator. Note that no single-qubit gates are

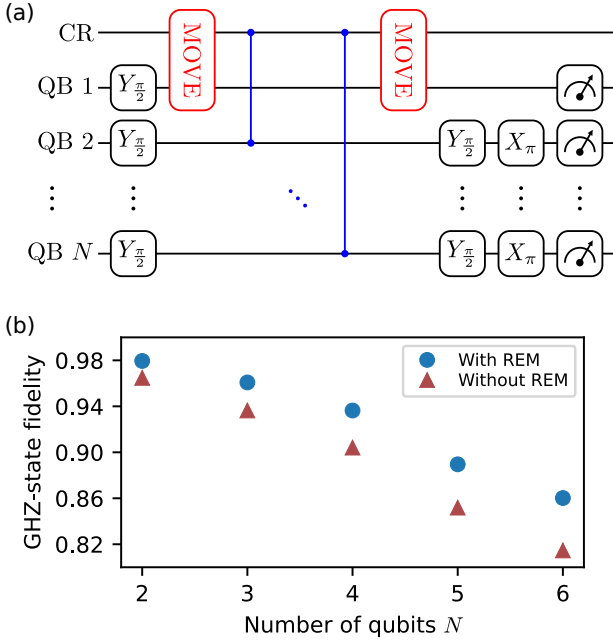


FIG. 4. GHZ state characterization. (a) Circuit for preparing a GHZ state with a variable number of entangled qubits N on a qubit-resonator QPU with star topology. (b) The fidelity $F_{|\psi\rangle_{\text{GHZ}}}$ is calculated from the GHZ state population and its coherence, inferred via multiple quantum coherences. We show the GHZ state fidelity as a function of the qubit number N , obtained by analysing the data both with (blue circles) and without (red triangles) applying readout-error mitigation.

applied to the MOVE qubit (QB 1 in Fig. 4 (a)) between the first and second MOVE operation. This ensures that this qubit is in the ground state when the second MOVE operation is applied.

A quantum state $|\psi\rangle$ is declared to be GME if the fidelity of the experimental state ρ with respect to the pure state is $F_{|\psi\rangle} = \langle\psi|\rho|\psi\rangle > 0.5$ [45]. We estimate the fidelity of the prepared GHZ state using the multiple quantum coherences method [46, 47] to certify its entanglement properties.

Fig. 4 (b) presents GHZ state fidelities both with and without readout-error mitigation (REM). The results successfully confirm the presence of GME for all six qubits, demonstrating that the entire device is entangled. Without mitigation, we obtain a GHZ state fidelity of $F_{|\psi\rangle_{\text{GHZ}}} = 0.815$. Furthermore, we mitigate readout errors by multiplying the raw readout results by the inverse of the readout assignment matrix, which includes both state preparation and measurement errors. The assignment matrix is a tensor product of all single-qubit assignment matrices and therefore assumes the readout errors to be completely uncorrelated. The mitigated GHZ fidelity for $N = 6$ qubits is $F_{|\psi\rangle_{\text{GHZ}}} = 0.86$.

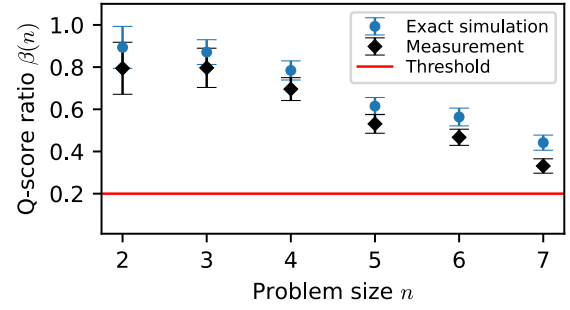


FIG. 5. Measured Q-score ratio as a function of problem size n . For each problem size, the average is taken over 60 randomly sampled Erdős–Rényi graphs. The error bars show the standard error of the mean.

B. Q-score Benchmark

In this section we assess the performance of the qubit-resonator QPU in solving combinatorial optimization problems. Specifically, we benchmark its ability to compute solutions for the maximum-cut problem using the Q-score benchmark [48]. The Q-score is defined for random *Erdős–Rényi graphs*, where each edge is included with probability $1/2$. A quantum processor passes the Q-score test for a given problem size n if it achieves a performance metric $\beta(n) \geq \beta^*$, where $\beta(n)$ quantifies the fraction of the optimality gap between a random guess and the optimal solution that is measured on the quantum system on average. If $\beta(n) = 1$, exact solutions are found, but if $\beta(n) = 0$, random solutions are found. Following Ref. [48], we take $\beta^* = 0.2$ meaning that the system passes the Q-score test for a given n if it performs on average 20% better than random guessing. Due to the accumulation of noise, passing the Q-score test becomes increasingly challenging as the problem size grows.

We evaluate Q-score performance $\beta(n)$ by using a depth $p = 1$ quantum approximate optimization algorithm (QAOA) circuit [49, 50], where the optimal circuit parameters are determined through analytical calculations [51]. By ensuring that the quantum processor operates with optimally pre-tuned parameters, we avoid expensive quantum-classical optimization loops and ensure the most efficient use of quantum resources. In the QAOA algorithm, the number of RZZ interactions equals the number of edges $|E|$ in the problem graph. As we consider random Erdős–Rényi graphs with edge probability $1/2$, we would need to implement on average $n(n-1)/2$ CZ gates on an all-to-all connected topology. We note that on a square-grid topology, we would require 50% to 75% more CZ gates for large n depending on which SWAP strategy is used [52]. This highlights the potential of the star topology in solving dense optimization tasks.

To further enhance performance, we execute quantum circuits on an optimized qubit layout, following the methodology introduced in [53]. This pre-processing step evaluates a noise score for each possible qubit layout,

considering the gate count of the circuit along with the single- and two-qubit gate error rates of the hardware. Furthermore, we apply readout-error mitigation using the *mtree package* [54], allowing us to exclude measurement errors from the noise score evaluation.

We demonstrate that our QPU passes the Q-score test for problem sizes defined across all $n = 6$ qubits of the QPU, as illustrated in Fig. 5. Additionally, we increase the Q-score to $n + 1 = 7$ by using the virtual node technique [55, 56], which breaks the \mathbb{Z}_2 -symmetry of the maximum-cut problem and introduces only a minor overhead from a few single-qubit Z -gates.

We note that for such small problem sizes, the CZ gate-count advantage of the star topology is rather small: e.g., for $n = 6$ we require on average 15 CZ gates on the star topology and 17 CZ gates on a square grid topology. In addition, we also need to implement $2(n-1)$ MOVE operations on the qubit-resonator star. For larger n , however, the gate-count advantage of the star topology becomes significant and approaches the asymptotic percentages stated above. Therefore, scaling up the qubit-resonator star topology is a worthwhile effort.

C. Jaynes-Cummings Gate to Access the Higher Resonator Levels

In the previous section, we have restricted the MOVE operation to the single-excitation manifold of the coupled qubit-resonator system to ensure that the resonator remains in the $\{|0\rangle, |1\rangle\}$ subspace. Here, we remove this restriction and populate higher resonator levels by applying the MOVE operation on the $|1, e\rangle$ state to verify that we are indeed implementing a Jaynes-Cummings gate as defined in Eq. (2). We construct circuits to investigate the dynamics of multiple resonator excitations $|n\rangle$ interfering with each other. With these interference fringes we measure and then correct non-ideal phases introduced by the MOVE operation to recover the dynamics of an ideal Jaynes-Cummings gate.

We can populate higher levels of the computational resonator by repeatedly employing the MOVE operation, thus providing additional computational degrees of freedom. In fact, exploiting the equidistant resonator energy spectrum can be used, for example, for digital quantum simulation [26] or for the implementation of the quantum Fourier transformation in oscillating modes. In the remainder of this section, we experimentally demonstrate how higher energy levels of the computational resonator can be accessed by applying successive MOVE operations, and we provide an exemplary circuit for phase calibration.

The MOVE operation is calibrated in the single photon manifold. For states containing n resonator photons, Eq. (2) predicts that the effective Rabi frequency increases characteristically as $\Omega_n = \sqrt{n}\Omega$ [57], implying swap angles exceeding $\pi/2$ and thus creation of superposition states containing $n \geq 2$ photons. In this case,

the JC interaction implements a mapping analogous to a fermionic simulation (fSim) gate [58, 59]. If the interaction is switched on for a gate time τ , the propagator corresponding to Eq. (1) leads to the general JC gate

$$\begin{aligned} |g, n\rangle &\rightarrow c_n^- |g, n\rangle - i s_n^+ |e, n-1\rangle, \\ |e, n\rangle &\rightarrow c_{n+1}^+ |e, n\rangle - i s_{n+1}^- |g, n+1\rangle, \end{aligned} \quad (4)$$

where

$$\begin{aligned} c_n^\pm &\equiv e^{-i(\gamma_n \pm \zeta_n)} \cos(\Omega_n \tau), \\ s_n^\pm &\equiv e^{-i(\gamma_n \pm \chi_n)} \sin(\Omega_n \tau). \end{aligned} \quad (5)$$

The phases γ_n, ζ_n and χ_n are single-qubit phases resulting from the dynamic frequency change of the involved components [60]. The calibration of the MOVE operation sets the constraint $\Omega\tau = \pi/2$.

A simple circuit for demonstrating the JC interaction by subsequent application of two MOVE operations between QB 3 and CR is shown in Fig. 6(a). A second idle qubit, QB 2, is read out to test for potential cross-talk and state leakage. The qubit-qubit population as well as the theoretically expected probabilities $P_{ee} = |s_2^\pm|^2 \simeq 0.63$ and $P_{eg} = |c_2^\pm|^2 \simeq 0.37$ are plotted in Fig. 6(c). We observe that the experimental data can be well explained by climbing the JC ladder, according to Eq. (4).

The aforementioned $|e, 1\rangle \leftrightarrow |g, 2\rangle$ population exchange experiment is independent of potential phase shifts in the two-photon manifold. This is not generally the case for circuits involving superposition states or excitation swaps between the computational resonator and different qubits. In a more general case involving superposition of states containing different resonator photon number or in case of JC interaction between the resonator and multiple qubits, the phases γ_n, ζ_n and χ_n need to be determined accurately, e.g., by the use of physical Z -rotations or Floquet theory [60]. These phase shifts depend on the flux pulse window and are required to be calibrated separately for each JC manifold to realize the ideal JC interaction. For the conventional MOVE operation, the only relevant phase, γ_1 , is compensated by employing a VZ rotation for the involved qubit drive signal. Correcting for these phase offsets in circuits leading to photon number contributions $n \geq 2$ requires additional control degrees of freedom such as physical Z -rotations.

An example for such a circuit is shown in Fig. 6(b). First, we move an excitation into the computational resonator using QB 3. Subsequently, we use QB 2 to implement a Ramsey sequence for the populated resonator. After the first (second) MOVE operation involving QB 2, we insert a physical Z -rotation Z_φ ($Z_{\varphi'}$). The frequency detuning Δ between QB 2 and CR induces a change of the rotating reference frame when the MOVE operation is applied. This change of reference frame induces a phase evolution proportional to the delay τ , manifesting as Ramsey oscillations. For the circuit in Fig. 6(b),

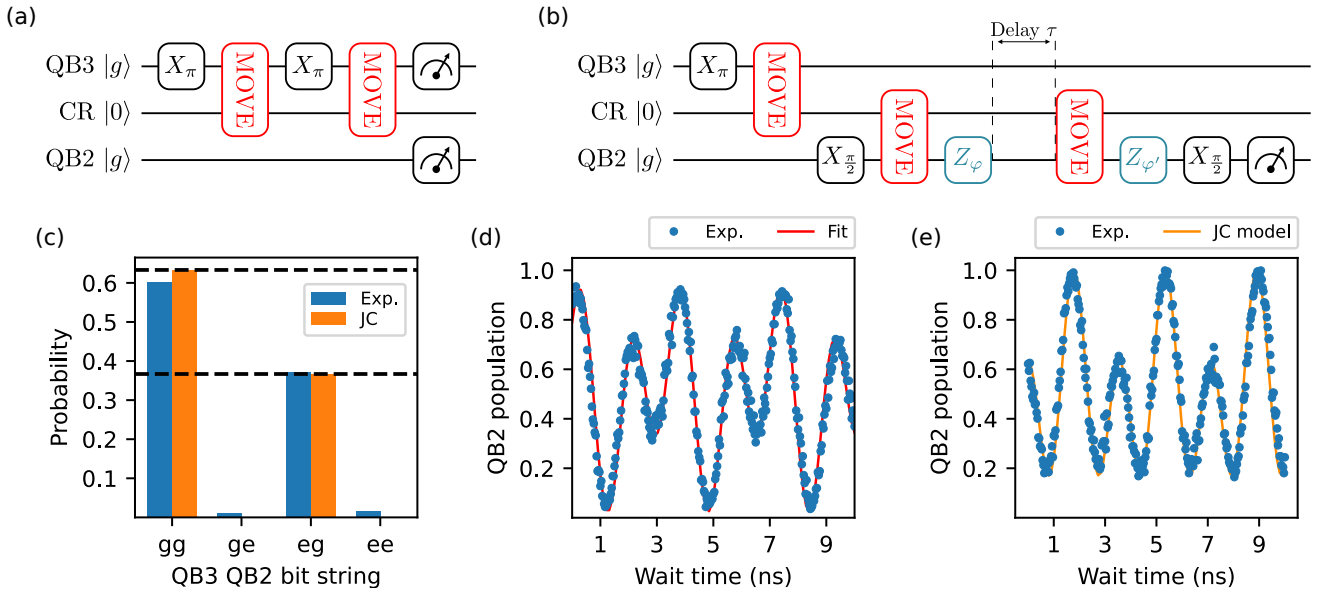


FIG. 6. (a) Quantum circuit to populate higher excited levels of the computational resonator by repeated excitation of QB 3, followed by application of the MOVE operation. In addition, a second idle qubit QB 2 is read out. (b) Circuit for measuring the free time evolution of the population of the first two excited computational resonator (CR) levels. After populating CR using QB 3, QB 2 is used to implement a Ramsey sequence which enables the measurement of the free resonator state evolution as a function of the delay time τ . The protocol additionally contains two physical Z -rotations, Z_φ and $Z_{\varphi'}$, which are used to compensate for phase offsets induced by the JC interaction. (c) Detected population of QB 3 and QB 2 (blue) for the circuit shown in panel (a) and comparison with the ideal JC model (orange). (d) Detected population of QB 2 as a function of τ (blue dots) for $\varphi = \varphi' = 0$. The red line corresponds to a fit according to Eq. (6). (e) QB 2 population as a function of τ (blue dots) after compensating all the phase offsets by employing physical Z -rotations φ and φ' . The orange line is the theoretical prediction from the ideal JC model.

the QB 2 population can be expressed as

$$P_e = \frac{1}{2} [1 - c_2^2 \cos(\Delta t + \phi) + s_2^2 \cos(2\Delta t + \phi')], \quad (6)$$

where $\phi \equiv -2\gamma_2 - 2\zeta_2 + \varphi'$ and $\phi' \equiv -2\gamma_2 + \varphi' - \varphi$. Consequently, in contrast to the conventional Ramsey experiment with an oscillation frequency Δ , we expect additional beating with frequency 2Δ due to the computational resonator state contributions from $n = 2$ during the free state evolution. Figure 6(d) shows the experimental result for the populated-resonator Ramsey experiment for detuning $\Delta/2\pi = 281$ MHz and $\varphi = \varphi' = 0$, as well as a fit according to Eq. (6). From the two fit parameters, $\phi = -2.73$ and $\phi' = -1.18$, we can determine the angles γ_2 and ζ_2 as well as the correct choice of φ and φ' to implement an ideal JC gate. The result from a subsequent experiment after employing the physical Z -corrections is shown in Fig. 6(e). Following this phase calibration, the circuit output can be well described by the ideal JC theory. These proof-of-principle results demonstrate that the JC gate phases can be controlled using physical Z -rotations. Additional information as well as the derivation of Eq. (6) is provided in Appendix G.

D. Error Mitigation to Improve Circuit Execution Reliability

The presence of noise in near-term quantum devices introduces significant errors in measured expectation values, limiting the accuracy of quantum computations. Error mitigation techniques provide a means to recover meaningful results without requiring additional hardware resources, making them a crucial component of practical quantum computation. We demonstrate that the presented QPU is fully compatible with the state-of-the-art and established error mitigation methods, which can substantially diminish the impact of the hardware noise on the quantum algorithm execution.

We focus on estimating the ground state energy of the transverse field Ising model (TFIM), a well-known system in quantum many-body physics. We consider this system in its critical phase (associated with a transverse field strength of $g = 1$) for a six-qubit system with periodic boundary conditions and nearest-neighbor connectivity. The Hamiltonian of the model is given by

$$H = -g \sum_j \sigma_X^j - \sum_{(i,j)} \sigma_Z^i \sigma_Z^j, \quad (7)$$

where the summation over (i, j) accounts for qubit pairs with direct interactions.

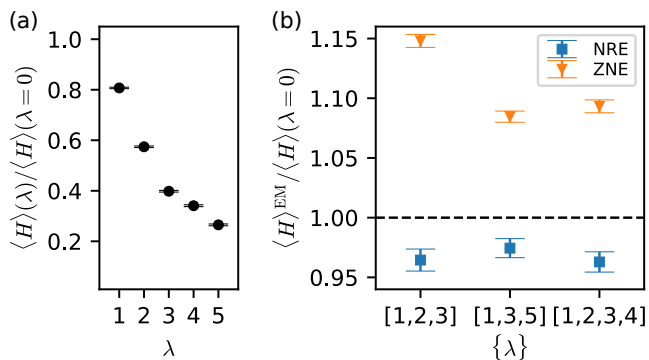


FIG. 7. (a) Measured ground-state energy of the TFIM, relative to its noise-free value, as a function of the noise scale factor λ . (b) Error-mitigated ground-state energy of the TFIM, relative to its noise-free value, obtained using NRE and ZNE for different choices of noise scale factors. In the case of ZNE, an exponential fitting procedure is employed. NRE is performed following the same approach outlined in [61]. Error bars for all error mitigated data points represent statistical uncertainties associated with a total of 240,000 measurement shots.

We estimate the ground-state energy with a variational approach based on QAOA with $p = 3$ layers [62]. The circuit parameters are optimized in a noise-free setting and subsequently transpiled to match the connectivity constraints and native gate set of the QPU. The resulting target circuit consists of 36 entangling CZ gates and 36 MOVE operations, which introduce noise and lead to errors in the measured energy expectation values.

To mitigate these errors, we employ a recently introduced algorithmic error mitigation technique known as noise-robust estimation (NRE) [61]. This method has been demonstrated to effectively recover noise-free expectation values with high accuracy, even without applying additional error-reduction techniques such as readout error mitigation or randomized compiling [63]. For comparison, we also apply the well-established zero-noise extrapolation (ZNE) method [64].

Both NRE and ZNE require amplification of hardware noise, necessitating the execution of the target circuit at different noise levels. Assuming that the circuit noise rate can be characterized by ϵ_0 , we parameterize the noise as $\epsilon = \lambda\epsilon_0$ where λ is the dimensionless noise scale factor. We realize different values of λ by using gate-level unitary folding [65]. This method amplifies noise by scaling the entire circuit unitary, U . For example, a noise amplification factor of $\lambda = 3$ is realized by replacing U with $UU^\dagger U$, increasing the circuit depth proportionally. For $\lambda = 2$, one first considers a unitary U_h that corresponds to a subset of the qubit operations, having half the depth of the original circuit. Then, U is replaced by

$UU_h^\dagger U_h$, introducing some unknown approximation error in the noise amplification process. Importantly, the performance of NRE is known to be largely insensitive to imprecise noise amplification [61]. This, in turn, relaxes the demanding requirement for precise noise amplification.

Figure 7(a) presents the measured ground-state energy as a function of noise scale factors. Due to inherent hardware noise, the measured energy is reduced by approximately 20% from its ideal noiseless value at $\lambda = 1$. In Fig. 7(b), we show the results after applying error mitigation with various different selections for noise scale factors. We find that NRE substantially improves the accuracy of noisy measurements of the QPU, yielding a final accuracy exceeding 96%, regardless of the specific noise amplification settings.

V. CONCLUSION

We have demonstrated a QPU based on qubits coupled to a common computational resonator. We have calibrated and benchmarked the qubit-resonator CZ gate and the MOVE operation, which, in combination with single-qubit gates, form a universal set of quantum gates. Furthermore, we have generated genuine multipartite entanglement between six qubits in the form of a GHZ state with a readout-error mitigated fidelity of 0.86 and provided a proof of principle demonstration on how to populate and calibrate higher level resonator states, eventually realizing a Jaynes-Cummings gate. Such a gate can be used as a building block for hybrid quantum computing schemes involving continuous and discrete variables [27]. In addition, we have shown a practical use case by employing our qubit-resonator QPU for QAOA applications including error mitigation. Finally, the presented proof of concept QPU shows a new paradigm for connectivity in superconducting architectures to match targeted applications. These include, for example, advanced quantum error correction strategies such as the color code [66–68].

Acknowledgments This work was supported by the German Federal Ministry of Education and Research through the projects DAQC (13N15686), QSolid (13N16155) and Q-Exa (13N16065).

Competing financial interests

The authors declare no competing financial interests.

Data availability

The data that support the findings of this study are available from the corresponding author upon reasonable request.

[1] L. Abdurakhimov, J. Adam, H. Ahmad, O. Ahoenen, M. Algaba, G. Alonso, V. Bergholm, R. Beriwal,

M. Beuerle, C. Bockstiegel, *et al.*, Technology and perfor-

- mance benchmarks of iqm's 20-qubit quantum computer (2024), arXiv:2408.12433 [quant-ph].
- [2] R. Acharya, D. A. Abanin, L. Aghababaie-Beni, I. Aleiner, T. I. Andersen, M. Ansmann, F. Arute, K. Arya, A. Asfaw, N. Astrakhantsev, *et al.*, Quantum error correction below the surface code threshold, *Nature* (2024).
- [3] J. B. Hertzberg, E. J. Zhang, S. Rosenblatt, E. Magesan, J. A. Smolin, J.-B. Yau, V. P. Adiga, M. Sandberg, M. Brink, J. M. Chow, *et al.*, Laser-annealing josephson junctions for yielding scaled-up superconducting quantum processors, *npj Quantum Information* **7**, 129 (2021).
- [4] M. Dupont, B. Evert, M. J. Hodson, B. Sundar, S. Jeffrey, Y. Yamaguchi, D. Feng, F. B. Maciejewski, S. Hadfield, M. S. Alam, *et al.*, Quantum-enhanced greedy combinatorial optimization solver, *Science Advances* **9**, eadi0487 (2023).
- [5] E. Dennis, A. Kitaev, A. Landahl, and J. Preskill, Topological quantum memory, *Journal of Mathematical Physics* **43**, 4452 (2002).
- [6] A. G. Fowler, M. Mariantoni, J. M. Martinis, and A. N. Cleland, Surface codes: Towards practical large-scale quantum computation, *Phys. Rev. A* **86**, 032324 (2012).
- [7] A. H. Karamlou, I. T. Rosen, S. E. Muschinske, C. N. Barrett, A. Di Paolo, L. Ding, P. M. Harrington, M. Hays, R. Das, D. K. Kim, *et al.*, Probing entanglement in a 2d hard-core bose–hubbard lattice, *Nature* **629**, 561 (2024).
- [8] Y. Kim, A. Eddins, S. Anand, K. X. Wei, E. van den Berg, S. Rosenblatt, H. Nayfeh, Y. Wu, M. Zaletel, K. Temme, and A. Kandala, Evidence for the utility of quantum computing before fault tolerance, *Nature* **618**, 500 (2023).
- [9] N. Lacroix, A. Bourassa, F. J. H. Heras, L. M. Zhang, J. Bausch, A. W. Senior, T. Edlich, N. Shutty, V. Sivak, A. Bengtsson, *et al.*, Scaling and logic in the color code on a superconducting quantum processor (2024), arXiv:2412.14256 [quant-ph].
- [10] F. Pan and P. Zhang, Simulation of quantum circuits using the big-batch tensor network method, *Phys. Rev. Lett.* **128**, 030501 (2022).
- [11] J. Tindall, M. Fishman, E. M. Stoudenmire, and D. Sels, Efficient tensor network simulation of ibm's eagle kicked ising experiment, *PRX Quantum* **5**, 010308 (2024).
- [12] X. Gao, M. Kalinowski, C.-N. Chou, M. D. Lukin, B. Barak, and S. Choi, Limitations of linear cross-entropy as a measure for quantum advantage, *PRX Quantum* **5**, 010334 (2024).
- [13] T. Begušić, J. Gray, and G. K.-L. Chan, Fast and converged classical simulations of evidence for the utility of quantum computing before fault tolerance, *Science Advances* **10**, eadk4321 (2024).
- [14] M. G. Algaba, M. Ponce-Martinez, C. Munuera-Javaloy, V. Pina-Canelles, M. J. Thapa, B. G. Taketani, M. Leib, I. de Vega, J. Casanova, and H. Heimonen, Co-design quantum simulation of nanoscale nmr, *Phys. Rev. Res.* **4**, 043089 (2022).
- [15] S. Bravyi, A. W. Cross, J. M. Gambetta, D. Maslov, P. Rall, and T. J. Yoder, High-threshold and low-overhead fault-tolerant quantum memory, *Nature* **627**, 778 (2024).
- [16] G. B. P. Huber, F. A. Roy, L. Koch, I. Tsitsilin, J. Schirk, N. J. Glaser, N. Bruckmoser, C. Schweizer, J. Romeiro, G. Krylov, *et al.*, Parametric multi-element coupling architecture for coherent and dissipative control of superconducting qubits (2024), arXiv:2403.02203 [quant-ph].
- [17] X. Wu, H. Yan, G. Andersson, A. Anferov, M.-H. Chou, C. R. Conner, J. Grebel, Y. J. Joshi, S. Li, J. M. Miller, *et al.*, Modular quantum processor with an all-to-all reconfigurable router, *Phys. Rev. X* **14**, 041030 (2024).
- [18] S. Hazra, A. Bhattacharjee, M. Chand, K. V. Salunkhe, S. Gopalakrishnan, M. P. Patankar, and R. Vijay, Ring-resonator-based coupling architecture for enhanced connectivity in a superconducting multiqubit network, *Physical Review Applied* **16**, 024018 (2021).
- [19] A. Wallraff, D. I. Schuster, A. Blais, L. Frunzio, R.-S. Huang, J. Majer, S. Kumar, S. M. Girvin, and R. J. Schoelkopf, Strong coupling of a single photon to a superconducting qubit using circuit quantum electrodynamics, *Nature* **431**, 162 (2004).
- [20] A. Blais, R.-S. Huang, A. Wallraff, S. M. Girvin, and R. J. Schoelkopf, Cavity quantum electrodynamics for superconducting electrical circuits: An architecture for quantum computation, *Physical Review A* **69**, 062320 (2004).
- [21] C. Song, K. Xu, W. Liu, C.-p. Yang, S.-B. Zheng, H. Deng, Q. Xie, K. Huang, Q. Guo, L. Zhang, *et al.*, 10-qubit entanglement and parallel logic operations with a superconducting circuit, *Physical Review Letters* **119** (2017).
- [22] C. Song, K. Xu, H. Li, Y.-R. Zhang, X. Zhang, W. Liu, Q. Guo, Z. Wang, W. Ren, J. Hao, *et al.*, Generation of multicomponent atomic schrödinger cat states of up to 20 qubits, *Science* **365**, 574–577 (2019).
- [23] M. Kjaergaard, M. E. Schwartz, J. Braumüller, P. Krantz, J. I.-J. Wang, S. Gustavsson, and W. D. Oliver, Superconducting qubits: Current state of play, *Annual Review of Condensed Matter Physics* **11**, 369 (2020).
- [24] S. Lloyd and S. L. Braunstein, Quantum computation over continuous variables, *Phys. Rev. Lett.* **82**, 1784 (1999).
- [25] S. L. Braunstein and P. van Loock, Quantum information with continuous variables, *Rev. Mod. Phys.* **77**, 513 (2005).
- [26] N. K. Langford, R. Sagastizabal, M. Kounalakis, C. Dickel, A. Bruno, F. Luthi, D. J. Thoen, A. Endo, and L. DiCarlo, Experimentally simulating the dynamics of quantum light and matter at deep-strong coupling, *Nature Communications* **8**, 1715 (2017).
- [27] Y. Liu, S. Singh, K. C. Smith, E. Crane, J. M. Martyn, A. Eickbusch, A. Schuckert, R. D. Li, J. Sinanan-Singh, M. B. Soley, *et al.*, Hybrid oscillator-qubit quantum processors: Instruction set architectures, abstract machine models, and applications (2024), arXiv:2407.10381 [quant-ph].
- [28] J. Leppäkangas, P. Stadler, D. Golubev, R. Reiner, J.-M. Reiner, S. Zanker, N. Wurz, M. Renger, J. Verjauw, D. Gusenkova, *et al.*, Quantum algorithms for simulating systems coupled to bosonic modes using a hybrid resonator-qubit quantum computer, [Manuscript in preparation] (2025).
- [29] Y. Sung, L. Ding, J. Braumüller, A. Vepsäläinen, B. Kannan, M. Kjaergaard, A. Greene, G. O. Samach, C. McNally, D. Kim, *et al.*, Realization of high-fidelity CZ and ZZ-free iSWAP gates with a tunable coupler, *Phys. Rev. X* **11**, 021058 (2021).
- [30] J. Koch, T. M. Yu, J. Gambetta, A. A. Houck, D. I.

- Schuster, J. Majer, A. Blais, M. H. Devoret, S. M. Girvin, and R. J. Schoelkopf, Charge-insensitive qubit design derived from the cooper pair box, *Phys. Rev. A* **76**, 042319 (2007).
- [31] F. Marxer, A. Vepsäläinen, S. W. Jolin, J. Tuorila, A. Landra, C. Ockeloen-Korppi, W. Liu, O. Ahonen, A. Auer, L. Belzane, *et al.*, Long-distance transmon coupler with cz-gate fidelity above 99.8%, *PRX Quantum* **4**, 010314 (2023).
- [32] F. Motzoi, J. M. Gambetta, P. Rebentrost, and F. K. Wilhelm, Simple pulses for elimination of leakage in weakly nonlinear qubits, *Physical review letters* **103**, 110501 (2009).
- [33] E. Hyyppä, A. Vepsäläinen, M. Papič, C. F. Chan, S. Inel, A. Landra, W. Liu, J. Luus, F. Marxer, C. Ockeloen-Korppi, *et al.*, Reducing leakage of single-qubit gates for superconducting quantum processors using analytical control pulse envelopes, *PRX Quantum* **5**, 030353 (2024).
- [34] J. M. Martinis, S. W. Nam, J. Aumentado, K. Lang, and C. Urbina, Decoherence of a superconducting qubit due to bias noise, *Physical Review B* **67**, 094510 (2003).
- [35] J. Bylander, S. Gustavsson, F. Yan, F. Yoshihara, K. Harrabi, G. Fitch, D. G. Cory, Y. Nakamura, J.-S. Tsai, and W. D. Oliver, Noise spectroscopy through dynamical decoupling with a superconducting flux qubit, *Nature Physics* **7**, 565–570 (2011).
- [36] D. C. McKay, C. J. Wood, S. Sheldon, J. M. Chow, and J. M. Gambetta, Efficient z gates for quantum computing, *Physical Review A* **96**, 022330 (2017).
- [37] F. Bao, H. Deng, D. Ding, R. Gao, X. Gao, C. Huang, X. Jiang, H.-S. Ku, Z. Li, X. Ma, *et al.*, Fluxonium: An alternative qubit platform for high-fidelity operations, *Physical review letters* **129**, 010502 (2022).
- [38] E. Magesan, J. M. Gambetta, B. R. Johnson, C. A. Ryan, J. M. Chow, S. T. Merkel, M. P. da Silva, G. A. Keefe, M. B. Rothwell, T. A. Ohki, *et al.*, Efficient measurement of quantum gate error by interleaved randomized benchmarking, *Phys. Rev. Lett.* **109**, 080505 (2012).
- [39] E. Knill, D. Leibfried, R. Reichle, J. Britton, R. B. Blakestad, J. D. Jost, C. Langer, R. Ozeri, S. Seidelin, and D. J. Wineland, Randomized benchmarking of quantum gates, *Phys. Rev. A* **77**, 012307 (2008).
- [40] H. Xiong, J. Wang, J. Song, J. Yang, Z. Bao, Y. Li, Z.-Y. Mi, H. Zhang, H.-F. Yu, Y. Song, and L. Duan, Scalable low-overhead superconducting non-local coupler with exponentially enhanced connectivity (2025), arXiv:2502.18902 [quant-ph].
- [41] S. Sheldon, L. S. Bishop, E. Magesan, S. Filipp, J. M. Chow, and J. M. Gambetta, Characterizing errors on qubit operations via iterative randomized benchmarking, *Phys. Rev. A* **93**, 012301 (2016).
- [42] T. Abad, J. Fernández-Pendás, A. Frisk Kockum, and G. Johansson, Universal fidelity reduction of quantum operations from weak dissipation, *Phys. Rev. Lett.* **129**, 150504 (2022).
- [43] T. Abad, Y. Schattner, A. F. Kockum, and G. Johansson, Impact of decoherence on the fidelity of quantum gates leaving the computational subspace (2024), arXiv:2302.13885 [quant-ph].
- [44] D. M. Greenberger, M. A. Horne, and A. Zeilinger, Going beyond bell’s theorem, in *Bell’s Theorem, Quantum Theory and Conceptions of the Universe*, edited by M. Kafatos (Springer Netherlands, Dordrecht, 1989) pp. 69–72.
- [45] T.-C. Wei and P. M. Goldbart, Geometric measure of entanglement and applications to bipartite and multipartite quantum states, *Phys. Rev. A* **68**, 042307 (2003).
- [46] K. X. Wei, I. Lauer, S. Srinivasan, N. Sundaresan, D. T. McClure, D. Toyli, D. C. McKay, J. M. Gambetta, and S. Sheldon, Verifying multipartite entangled Greenberger-Horne-Zeilinger states via multiple quantum coherences, *Phys. Rev. A* **101**, 032343 (2020).
- [47] J. Baum, M. Munowitz, A. N. Garroway, and A. Pines, Multiple-quantum dynamics in solid state NMR, *The Journal of Chemical Physics* **83**, 2015 (1985).
- [48] S. Martiel, T. Ayril, and C. Allouche, Benchmarking quantum coprocessors in an application-centric, hardware-agnostic, and scalable way, *IEEE Transactions on Quantum Engineering* **2**, 1 (2021).
- [49] E. Farhi, J. Goldstone, and S. Gutmann, A quantum approximate optimization algorithm (2014).
- [50] K. Bharti, A. Cervera-Lierta, T. H. Kyaw, T. Haug, S. Alperin-Lea, A. Anand, M. Degroote, H. Heimonen, J. S. Kottmann, T. Menke, *et al.*, Noisy intermediate-scale quantum algorithms, *Rev. Mod. Phys.* **94**, 015004 (2022).
- [51] A. Ozaeta, W. van Dam, and P. L. McMahon, Expectation values from the single-layer quantum approximate optimization algorithm on ising problems, *Quantum Sci. Technol.* **7**, 045036 (2022) **7**, 045036 (2020).
- [52] J. Weidenfeller, L. C. Valor, J. Gacon, C. Tornow, L. Bello, S. Woerner, and D. J. Egger, Scaling of the quantum approximate optimization algorithm on superconducting qubit based hardware, *Quantum* **6**, 870 (2022).
- [53] P. D. Nation and M. Treinish, Suppressing quantum circuit errors due to system variability, *PRX Quantum* **4**, 010327 (2023).
- [54] P. D. Nation, H. Kang, N. Sundaresan, and J. M. Gambetta, Scalable mitigation of measurement errors on quantum computers, *PRX Quantum* **2**, 040326 (2021).
- [55] S. Bravyi, A. Kliesch, R. Koenig, and E. Tang, Obstacles to variational quantum optimization from symmetry protection, *Physical review letters* **125**, 260505 (2020).
- [56] J. Rönkkö, O. Ahonen, V. Bergholm, A. Calzona, A. Geresdi, H. Heimonen, J. Heinsoo, V. Milchakov, S. Pogorzalek, M. Sarsby, *et al.*, On-premises superconducting quantum computer for education and research, *EPJ Quantum technology* **11**, 32 (2024).
- [57] J. M. Fink, M. Göppl, M. Baur, R. Bianchetti, P. J. Leek, A. Blais, and A. Wallraff, Climbing the jaynes-cummings ladder and observing its nonlinearity in a cavity qed system, *Nature* **454**, 315 (2008).
- [58] F. Arute, K. Arya, R. Babbush, D. Bacon, J. C. Bardin, R. Barends, R. Biswas, S. Boixo, F. G. S. L. Brandao, D. A. Buell, *et al.*, Quantum supremacy using a programmable superconducting processor, *Nature* **574**, 505 (2019).
- [59] H.-F. Wang, A.-D. Zhu, S. Zhang, and K.-H. Yeon, Simple implementation of discrete quantum fourier transform via cavity quantum electrodynamics, *New Journal of Physics* **13**, 013021 (2011).
- [60] F. Arute, K. Arya, R. Babbush, D. Bacon, J. C. Bardin, R. Barends, A. Bengtsson, S. Boixo, M. Broughton, B. B. Buckley, *et al.*, Observation of separated dynamics of charge and spin in the fermi-hubbard model (2020), arXiv:2010.07965 [quant-ph].

- [61] A. Hosseinkhani, F. Šimkovic, A. Calzona, T. Liu, A. Auer, and I. de Vega, Noise-robust estimation of quantum observables in noisy hardware (2025), arXiv:2503.06695 [quant-ph].
- [62] W. W. Ho and T. H. Hsieh, Efficient variational simulation of non-trivial quantum states, *SciPost Phys.* **6**, 029 (2019).
- [63] A. Hashim, R. K. Naik, A. Morvan, J.-L. Ville, B. Mitchell, J. M. Kreikebaum, M. Davis, E. Smith, C. Iancu, K. P. O’Brien, *et al.*, Randomized compiling for scalable quantum computing on a noisy superconducting quantum processor, *Phys. Rev. X* **11**, 041039 (2021).
- [64] A. Kandala, K. Temme, A. D. Córcoles, A. Mezzacapo, J. M. Chow, and J. M. Gambetta, Error mitigation extends the computational reach of a noisy quantum processor, *Nature* **567**, 491–495 (2019).
- [65] K. Schultz, R. LaRose, A. Mari, G. Quiroz, N. Shammah, B. D. Clader, and W. J. Zeng, Impact of time-correlated noise on zero-noise extrapolation, *Phys. Rev. A* **106**, 052406 (2022).
- [66] H. Bombin and M. A. Martin-Delgado, Topological quantum distillation, *Phys. Rev. Lett.* **97**, 180501 (2006).
- [67] A. J. Landahl, J. T. Anderson, and P. R. Rice, Fault-tolerant quantum computing with color codes (2011), arXiv:1108.5738 [quant-ph].
- [68] Y. Takada and K. Fujii, Improving threshold for fault-tolerant color-code quantum computing by flagged weight optimization, *PRX Quantum* **5**, 030352 (2024).
- [69] F. Yan, P. Krantz, Y. Sung, M. Kjaergaard, D. L. Campbell, T. P. Orlando, S. Gustavsson, and W. D. Oliver, Tunable coupling scheme for implementing high-fidelity two-qubit gates, *Phys. Rev. Appl.* **10**, 054062 (2018).
- [70] L. Heunisch, C. Eichler, and M. J. Hartmann, Tunable coupler to fully decouple and maximally localize superconducting qubits, *Phys. Rev. Appl.* **20**, 064037 (2023).
- [71] M. Papič, J. Tuorila, A. Auer, I. de Vega, and A. Hosseinkhani, Charge-parity switching effects and optimisation of transmon-qubit design parameters, *npj Quantum Information* **10** (2024).
- [72] M. Scully and M. Zubairy, *Quantum Optics*, Quantum Optics (Cambridge University Press, 1997).
- [73] Y. Chu, P. Kharel, W. H. Renninger, L. D. Burkhardt, L. Frunzio, P. T. Rakich, and R. J. Schoelkopf, Quantum acoustics with superconducting qubits, *Science* **358**, 199 (2017).
- [74] M. Mariantoni, E. P. Menzel, F. Deppe, M. A. Araque Caballero, A. Baust, T. Niemczyk, E. Hoffmann, E. Solano, A. Marx, and R. Gross, Planck spectroscopy and quantum noise of microwave beam splitters, *Phys. Rev. Lett.* **105**, 133601 (2010).
- [75] S. Gandorfer, M. Renger, W. Yam, F. Fesquet, A. Marx, R. Gross, and K. Fedorov, Two-dimensional planck spectroscopy for microwave photon calibration, *Physical Review Applied* **23** (2025).
- [76] S. Boixo, S. V. Isakov, V. N. Smelyanskiy, R. Babbush, N. Ding, Z. Jiang, M. J. Bremner, J. M. Martinis, and H. Neven, Characterizing quantum supremacy in near-term devices, *Nature Physics* **14**, 595 (2018).

Appendix A: Experimental Setup

Figure S8 illustrates the experimental setup with a simplified QPU circuit diagram featuring one qubit QB (including its readout resonator RO and Purcell filter), the computational resonator CR and a tunable coupler TC that couples the qubit to the computational resonator. The QPU and some electrical components are maintained at cryogenic temperature in a Bluefors XLD400 cryostat. The control electronics instruments, at room temperature, are connected to the QPU via coaxial cables. These contain microwave attenuators and filters distributed over the various temperature stages of the cryostat. Flux pulses and flux biases are generated by arbitrary waveform generators AWG (Zurich Instrument HDAWG8), the qubit drive pulses are generated by signal generators SG (Zurich Instrument SHFQC6+), and the readout pulses are generated and acquired by a quantum analyzer QA (contained in the same SHFQC6+ instrument). Before digitization, the readout pulses are amplified by a cryogenic amplifier based on a high electron mobility transistor HEMT and a warm amplifier WAMP. A group of isolators protects the readout resonator from noise.

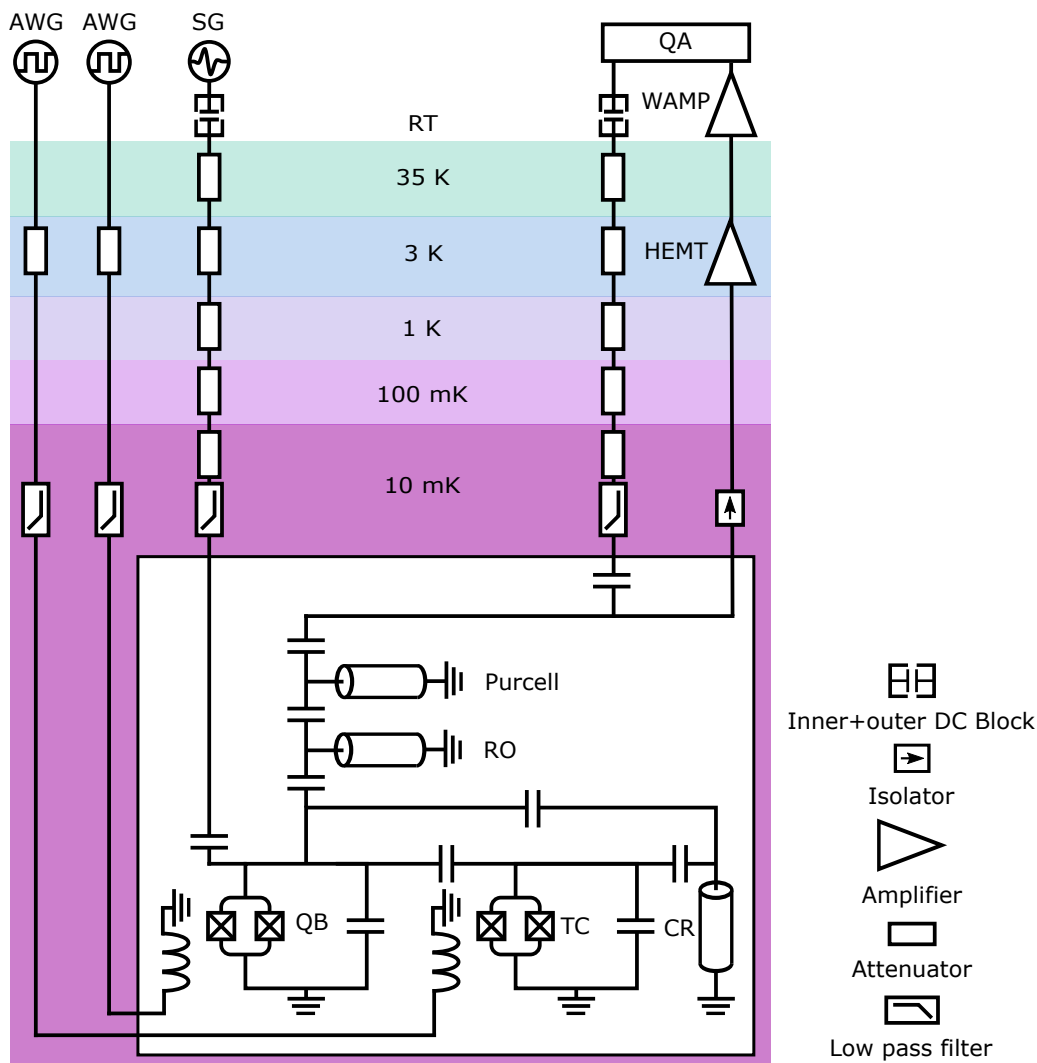


Figure S8. Experiment setup schematically depicting the QPU in its cryogenic environment. The QPU is connected via coaxial lines to control electronics at room temperature. The temperature of each stage is indicated.

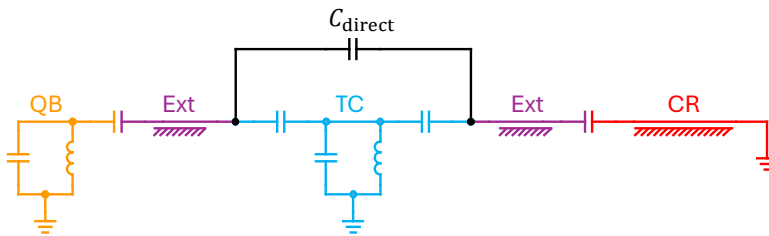


Figure S9. Simplified linearized circuit diagram of the QPU, showing a single qubit (QB) coupled via a tunable coupler (TC) to the computational resonator (CR). The couplings are mediated by coupler extender waveguides (Ext). The direct capacitance C_{direct} is part of the TC geometry, and ensures that there is an idling configuration where the ZZ interaction is zero. The remaining five qubits are connected to the CR in a similar fashion, each with a similar TC. In the model, each node also contains a parasitic capacitance to ground, which is omitted from the drawing for clarity.

Appendix B: QPU Design

We model the star topology QPU including the computational resonator, six tunable couplers and six qubits as a linearized circuit, where the superconducting quantum interference devices (SQUIDs) have been replaced by linear inductors, as shown schematically for a single QB-TC-CR connection in Figure S9. Here, the localized qubit and coupler islands are modeled as pure capacitive structures (including a capacitance to ground at each island) extracted from finite element simulations of the respective geometry. The TC are coupled with interdigital capacitors near the open-circuit end of the CR. The QB-TC and TC-CR connections are formed by coupler extender waveguides, similar to those used in Ref. [S31], which enable physically spacing out the qubits while still coupling them all near the maximum voltage of the computational resonator mode. The coupler extender waveguides and the computational resonator are modeled as transmission lines to accurately include their inductive contributions. All elements are referenced to a common ground plane in the design and the model.

We extract the mode frequencies in this model from the divergences of the frequency-dependent impedance $Z(\omega)$ calculated at the respective qubit or coupler island, or for the CR at its open end. We use the following procedure to numerically estimate the frequencies and coupling strengths of the full six-qubit star system. First, we tune all QB and TC modes far away from the resonator mode by adjusting their inductance values, and from the remaining model extract the bare resonator frequency $\omega_r = 4.3$ GHz. Then, we pairwise tune two modes on co-resonance, while tuning all remaining modes far away, and extract the corresponding normalized coupling strength $\beta_{ij} = g_{ij}/\omega$ from the frequency splitting $2g_{ij}$. For tuning the CR mode, we adjust the modelled transmission line length. Table S1 shows the modeled and experimentally measured coupling strengths.

Parameter	Description	QB 1	QB 2	QB 3	QB 4	QB 5	QB 6
β_{qc}	Design model	0.0226	0.0226	0.0226	0.0226	0.0230	0.0230
β_{cr}		0.0225	0.0225	0.0226	0.0226	0.0225	0.0225
β_{qr}	Experimentally measured	0.0020	0.0020	0.0020	0.0020	0.0020	0.0020
β_{qc}		0.017	0.022	0.021	0.021	0.021	0.022

Table S1. Coupler parameters extracted from the design model, and for QB-TC couplings measured experimentally. The subscripts q , c and r represent the QB, TC and CR, respectively.

Appendix C: Fabrication

The quantum processing units (QPUs) were fabricated at the OtaNano Micronova cleanroom. A high-resistivity ($\rho > 10$ k Ω cm) n-type undoped (100) 6-inch silicon wafer, pre-cleaned to ensure a nonoxidized surface, served as the substrate. A 200-nm-thick high-purity niobium (Nb) layer was first deposited via sputtering to form the base superconducting circuit layer. Coplanar waveguides and capacitive structures were patterned using photolithography with a mask aligner, followed by reactive ion etching (RIE) to define the Nb features. Post-etching photoresist residuals were removed via ultrasonic cleaning in acetone and isopropanol (IPA), followed by nitrogen drying. Josephson junctions for the transmon qubits were fabricated on individual dice via electron-beam lithography (EBL). A bilayer of methylmethacrylate/polymethylmethacrylate (MMA/PMMA) resist was employed, with development in a sequence of methyl isobutyl ketone (MIBK):IPA (1:3), methyl glycol, and IPA. Residual resist was removed via a oxygen plasma

descum process. The junctions were fabricated using electron-beam shadow evaporation technique, depositing two aluminum (Al) layers under ultrahigh vacuum. Lift-off in heated acetone finalized the junction structures. Airbridges for interlayer connections were formed by Al, followed by a second lift-off process. Post-fabrication, the room-temperature resistance of the Josephson junctions was measured to verify junction integrity prior to cryogenic characterization. This process integrates high-yield lithography, contamination-minimized etching, and precise junction fabrication, ensuring robust superconducting circuits for quantum computing applications.

Appendix D: Schrieffer–Wolff Transformation

We consider here the approximate diagonalization of a setup that can be modelled with the Hamiltonian

$$\hat{H} = \hat{H}_0 + \hat{V}, \quad (\text{S1})$$

where \hat{H}_0 is an uncoupled (diagonal) Hamiltonian, and \hat{V} is a Hermitian operator describing the interactions between the eigenstates of \hat{H}_0 . In particular, we concentrate on a system which comprises a qubit, a resonator, and a tunable coupler. Consequently, the unperturbed Hamiltonian can be written as

$$\hat{H}_0 = \hbar\omega_q \hat{a}_q^\dagger \hat{a}_q + \frac{\hbar}{2} \alpha_q \hat{a}_q^\dagger \hat{a}_q^\dagger \hat{a}_q \hat{a}_q + \hbar\omega_r \hat{a}_r^\dagger \hat{a}_r + \hbar\omega_c \hat{a}_c^\dagger \hat{a}_c + \frac{\hbar}{2} \alpha_c \hat{a}_c^\dagger \hat{a}_c^\dagger \hat{a}_c \hat{a}_c, \quad (\text{S2})$$

where ω_q , ω_r and ω_c are the (angular) frequencies of the qubit, resonator and coupler, respectively, α_q is the anharmonicity of the qubit, α_c is the anharmonicity of the coupler, and \hat{a}_i and \hat{a}_i^\dagger are the annihilation and creation operators for the qubit, resonator and coupler, respectively, for $i \in \{q, r, c\}$. The interaction part $\hat{V} = \hat{V}_1 + \hat{V}_2$ describes the couplings between the qubit, resonator and coupler degrees of freedom. We have defined the interaction Hamiltonians as

$$\begin{aligned} \hat{V}_1 &= -\hbar g_{qc} (\hat{a}_q^\dagger - \hat{a}_q) (\hat{a}_c^\dagger - \hat{a}_c) - \hbar g_{rc} (\hat{a}_r^\dagger - \hat{a}_r) (\hat{a}_c^\dagger - \hat{a}_c), \\ \hat{V}_2 &= -\hbar g_{qr} (\hat{a}_q^\dagger - \hat{a}_q) (\hat{a}_r^\dagger - \hat{a}_r). \end{aligned} \quad (\text{S3})$$

Above, we denote the coupling strength between the qubit and the resonator with g_{qr} , the coupling strength between the qubit and the coupler with g_{qc} , and the coupling strength between the resonator and the coupler with g_{rc} .

Here, we assume that coupling to the coupler is dispersive, i.e., $g_{qc} \ll |\Delta_{qc}|$ and $g_{rc} \ll |\Delta_{rc}|$. However, we do not make such assumption for the qubit-resonator coupling g_{qr} . Since the coupler is in the dispersive limit, we make a Schrieffer–Wolff transformation $\hat{U}_{\text{SW}} = e^{\hat{S}}$ in order to eliminate the first-order interaction \hat{V}_1 with the coupler, and consequently obtain an effective Hamiltonian for the qubit-resonator system. In general, the Schrieffer–Wolff transformation can be expanded using the Baker–Campbell–Hausdorff lemma as

$$\hat{U}_{\text{SW}} \hat{H} \hat{U}_{\text{SW}}^\dagger = \hat{H} + [\hat{S}, \hat{H}] + \frac{1}{2!} [\hat{S}, [\hat{S}, \hat{H}]] + \dots \quad (\text{S4})$$

Here, we assume that $[\hat{S}, \hat{H}_0 + \hat{V}_2] = -\hat{V}_1$, which removes the first-order dependence on \hat{V}_1 from the transformed Hamiltonian. The condition obtained above is fulfilled in our setup if we write $\hat{S} = \hat{S}_q + \hat{S}_r$, and define [S69, S70]

$$\begin{aligned} \hat{S}_q &= \sum_{n_q, n_c \in \{0,1\}} \sqrt{(n_q + 1)(n_c + 1)} \left[\frac{g_{qc}}{\Delta_{qc} + n_q \alpha_q - n_c \alpha_c} (\hat{\pi}_q^{n_q+1, n_q} \hat{\pi}_c^{n_c, n_c+1} - \hat{\pi}_q^{n_q, n_q+1} \hat{\pi}_c^{n_c+1, n_c}) \right. \\ &\quad \left. - \frac{g_{qc}}{\Sigma_{qc} + n_q \alpha_q + n_c \alpha_c} (\hat{\pi}_q^{n_q+1, n_q} \hat{\pi}_c^{n_c+1, n_c} - \hat{\pi}_q^{n_q, n_q+1} \hat{\pi}_c^{n_c, n_c+1}) \right], \\ \hat{S}_r &= \sum_{n_r, n_c \in \{0,1\}} \sqrt{(n_r + 1)(n_c + 1)} \left[\frac{g_{rc}}{\Delta_{rc} - n_c \alpha_c} (\hat{\pi}_r^{n_r+1, n_r} \hat{\pi}_c^{n_c, n_c+1} - \hat{\pi}_r^{n_r, n_r+1} \hat{\pi}_c^{n_c+1, n_c}) \right. \\ &\quad \left. - \frac{g_{rc}}{\Sigma_{rc} + n_c \alpha_c} (\hat{\pi}_r^{n_r+1, n_r} \hat{\pi}_c^{n_c+1, n_c} - \hat{\pi}_r^{n_r, n_r+1} \hat{\pi}_c^{n_c, n_c+1}) \right], \end{aligned} \quad (\text{S5})$$

where the operators $\hat{\pi}_k^{n,m} = |n\rangle\langle m|$ act in the Hilbert space of $k \in \{q, r, c\}$, and we have defined $\Delta_{rc} = \omega_r - \omega_c$, $\Delta_{qc} = \omega_q - \omega_c$, $\Sigma_{qc} = \omega_q + \omega_c$ and $\Sigma_{rc} = \omega_r + \omega_c$. Consequently, the transformed Hamiltonian can be written in second order in the coupling strengths as

$$\hat{U}_{\text{SW}} \hat{H} \hat{U}_{\text{SW}}^\dagger = \hat{H}_0 + \hat{V}_2 + \frac{1}{2} [\hat{S}, \hat{V}_1], \quad (\text{S7})$$

In our architecture, we typically consider that coupling strength g_{qr} is almost an order of magnitude smaller than g_{qc} and g_{rc} .

After performing the Schrieffer–Wolff transformation [evaluating Eq. (S7)], we obtain corrections to qubit and resonator frequencies and effective couplings between the relevant (coupler-dressed) states that govern the MOVE and CZ operations. By additionally setting the energy of the ground state to zero, we obtain that the qubit and resonator frequencies and the effective couplings between the relevant single- and two-excitation eigenstates can be written as

$$\tilde{\omega}_q = \omega_q + \frac{g_{qc}^2}{\Delta_{qc}} - \frac{2g_{qc}^2}{\Sigma_{qc} + \alpha_q} + \frac{g_{qc}^2}{\Sigma_{qc}}, \quad (\text{S8})$$

$$\tilde{\omega}_r = \omega_r + \frac{g_{rc}^2}{\Delta_{qc}} - \frac{g_{rc}^2}{\Sigma_{rc}}, \quad (\text{S9})$$

$$\tilde{g}_{0e,1g} = g_{qr} + \frac{g_{qc}g_{rc}}{2} \left(\frac{1}{\Delta_{qc}} + \frac{1}{\Delta_{rc}} - \frac{1}{\Sigma_{qc}} - \frac{1}{\Sigma_{rc}} \right), \quad (\text{S10})$$

$$\tilde{g}_{1e,2g} = \sqrt{2}\tilde{g}_{0e,1g}, \quad (\text{S11})$$

$$\tilde{g}_{1e,0f} = \sqrt{2} \left[g_{qr} + \frac{g_{qc}g_{rc}}{2} \left(\frac{1}{\Delta_{rc}} + \frac{1}{\Delta_{qc} + \alpha_q} - \frac{1}{\Sigma_{rc}} - \frac{1}{\Sigma_{qc} + \alpha_q} \right) \right]. \quad (\text{S12})$$

Here, we have defined that $\tilde{g}_{0e,1g}$ is the coupling strength between the (coupler-dressed) states $|eg0\rangle$ and $|gg1\rangle$, $\tilde{g}_{1e,2g}$ between the states $|eg1\rangle$ and $|gg2\rangle$ and $\tilde{g}_{1e,0f}$ between the states $|eg1\rangle$ and $|fg0\rangle$ (state labelling goes as [qubit, coupler, resonator]). We assume here that the coupler is in the ground state. Furthermore, we also assume that the qubit and coupler frequencies are constant and, thus, the relations obtained above are a good approximation only for idling gates or for longer (adiabatic) gates dominated by a long interaction time. Our effective Hamiltonian (not shown) also includes other non-zero terms that couple states, such as $|gg0\rangle$ to $|eg1\rangle$ and $|gg0\rangle$ to $|gg2\rangle$, but these leakage transitions can be neglected under the rotating-wave approximation. The effective coupling strengths $\tilde{g}_{0e,1g}$ and $\tilde{g}_{1e,0f}$ are responsible for the MOVE and CZ gate dynamics, and from hereafter we refer to them as \tilde{g}_{MOVE} and \tilde{g}_{CZ} , respectively. We note that Eq. (S11) indicates that populating the $|eg1\rangle$ state during the MOVE gate results in undesired population transfer to the $|gg2\rangle$ state which is outside of the computational subspace. Furthermore, Eq. (S11) and Eq. (S12) can be further generalised. For n photons in the resonator, the effective coupling strengths can be written as $\tilde{g}_{(n-1)e,ng} = \sqrt{n}\tilde{g}_{0e,1g}$ and $\tilde{g}_{ne,(n-1)f} = \sqrt{n}\tilde{g}_{1e,0f}$. As is the case in the Jaynes-Cummings physics, coupling strengths are seen to scale with the photon number as \sqrt{n} .

Utilising Eq. (S12) and truncating the Hamiltonian in Eq. (S7) to a 5-level subspace spanned by $\{|gg0\rangle, |eg0\rangle, |gg1\rangle, |eg1\rangle, |fg0\rangle\}$, we obtain analytical expressions for the population and conditional phase for the $|eg1\rangle$ state during the CZ gate operation. In doing so, we assume that the leakage outside of the truncated subspace is negligible, and that at the CZ gate operational point, i.e., at $\tilde{\omega}_q = \tilde{\omega}_r - \alpha_q$, the single-excitation swapping \tilde{g}_{MOVE} can be neglected because $|\tilde{\omega}_q - \tilde{\omega}_r| \gg \tilde{g}_{\text{MOVE}}$. We obtain the effective time-evolution operator as $\hat{U} = \exp(-i\tilde{H}t)$, where \tilde{H} is the truncated Hamiltonian in the coupler-dressed eigenbasis and, by applying it to the initial $|eg1\rangle$ state, we obtain that the population in the state $|eg1\rangle$ can be written as [S71]

$$P_{|eg1\rangle}(t) = 1 - \frac{2\tilde{g}_{\text{CZ}}^2}{\tilde{\Omega}^2} \left[1 - \cos(\tilde{\Omega}t) \right], \quad (\text{S13})$$

where $\tilde{\Omega} = \sqrt{(\tilde{\Delta} - \alpha_q)^2 + 4\tilde{g}_{\text{CZ}}^2}$ and $\tilde{\Delta} = \tilde{\omega}_r - \tilde{\omega}_q$. Eq. (S13) suggests that during the CZ gate, the population periodically returns to the $|eg1\rangle$ state exhibiting the Rabi physics [S72].

The conditional phase that the state $|eg1\rangle$ picks up during the CZ gate can also be analytically extracted and is given as [S71]

$$\phi(t) = \frac{1}{2} \left[(\alpha_q - \tilde{\Delta})t + \pi \left(1 - \text{sign}\{\cos(\tilde{\Omega}t/2)\} \right) \right] + \arctan \left(\frac{\tilde{\Delta} - \alpha_q}{\tilde{\Omega}} \tan(\tilde{\Omega}t/2) \right). \quad (\text{S14})$$

In the experiment, the gate time τ_{CZ} is fixed, and $\tilde{\Delta}$ and $\tilde{\Omega}$ are tuned via the amplitudes of the qubit and coupler flux pulses such that $\phi(\tau_{\text{CZ}}) = \pi$.

Appendix E: Calibration and Benchmarking

We summarize the QPU calibration data in Tab.S2. The data for the coherence times, readout fidelity, and single-qubit gate fidelity has been taken over a time frame of 238 hours. The statistics consist of 208 data points for

the coherence times, 210 data points for the readout fidelity and 49 data points for the single-qubit gate fidelities, which have been characterized individually and simultaneously on all qubits. In between the individual benchmarking measurements, the QPU has been recalibrated by an automatic service. The Josephson energy E_J has been determined by fitting the coupler flux dispersion. The energy ratio E_J/E_C is determined by using the design parameters for the charging energy E_C . The individual gate fidelities for the MOVE operation and for the CZ gate are shown in Tab. S3. The error bars are determined from the corresponding fit errors by error propagation. We implement single-qubit gates using the derivative removal by adiabatic gate (DRAG) method with a cosine shaped envelope of the in-phase component [S32]. For the MOVE operation and for the CZ gate, we use cosine flux pulses on the qubits and square pulses smoothed by truncated Gaussian ramps for the tunable couplers. The respective gate durations, including buffer time to account for residual flux pulse distortions affecting the performance of the qubit-resonator operations, are summarized in Tab. S4.

Parameter	Description	QB 1	QB 2	QB 3	QB 4	QB 5	QB 6	CR
f_q (GHz)	Qubit/resonator frequency	4.67	4.47	4.41	4.52	4.63	4.93	4.22
T_1 (μ s)	Lifetime	25.6 ± 4.1	44.0 ± 5.3	55.3 ± 1.1	46.2 ± 9.0	45.9 ± 8.6	30.6 ± 5.6	5.53 ± 0.32
T_2^* (μ s)	Dephasing time	36.5 ± 6.1	27.1 ± 3.4	29.0 ± 4.3	22.2 ± 2.0	51.5 ± 9.9	31.9 ± 8.2	10.9 ± 1.0
T_2^e (μ s)	Hahn echo dephasing time	44.2 ± 7.1	56.0 ± 5.5	42.3 ± 4.5	29.9 ± 2.2	58.6 ± 8.8	43.8 ± 8.1	
T_q (mK)	Effective qubit temperature	46.3	42.0	43.6	40.9	43.0	45.8	
E_J/h (GHz)	Josephson energy	14.8	13.8	13.3	13.9	14.6	16.5	
E_J/E_C	Energy ratio	74.2	68.8	66.5	69.6	73.0	82.3	
F_{RO} (%)	Readout fidelity	98.3 ± 0.3	98.6 ± 0.2	98.7 ± 0.3	99.1 ± 0.2	98.9 ± 0.2	98.7 ± 0.6	
$F_{sq,ind}$ (%)	Individual SQG fidelity	99.93 ± 0.02	99.94 ± 0.04	99.96 ± 0.02	99.96 ± 0.01	99.96 ± 0.01	99.89 ± 0.3	
$F_{sq,sim}$ (%)	Simultaneous SQG fidelity	99.93 ± 0.02	99.92 ± 0.04	99.96 ± 0.03	99.95 ± 0.01	99.59 ± 0.01	99.87 ± 0.3	

Table S2. QPU performance. If provided, the uncertainty corresponds to the empirical standard deviation measured over a 238 h period. For the qubit/resonator frequency, the standard deviation is on the order of 10 kHz.

Parameter	Description	QB 1	QB 2	QB 3	QB 4	QB 5	QB 6
F_m (%)	Double MOVE fidelity	99.11 ± 0.05	99.34 ± 0.03	99.00 ± 0.03	99.30 ± 0.03	98.31 ± 0.06	97.95 ± 0.10
F_{cz} (%)	CZ fidelity	98.90 ± 0.05	98.75 ± 0.04	98.97 ± 0.03	98.04 ± 0.08	98.53 ± 0.14	96.61 ± 0.05

Table S3. Individual double MOVE and CZ fidelities.

Parameter	Description	QB 1	QB 2	QB 3	QB 4	QB 5	QB 6
τ_s (ns)	Single-qubit gate duration	40	40	40	40	40	40
τ_m (ns)	MOVE operation duration	88	80	96	80	96	96
τ_{cz} (ns)	CZ gate duration	96	80	80	112	96	80

Table S4. Duration of single-qubit and qubit-resonator operations.

1. Calibration of the MOVE Operation

The initial calibration of the MOVE operation is presented in the main text, therefore only the fine calibration of the operating point and the calibration of the single-qubit phase correction of the MOVE operation are discussed here. The fine calibration experiment for the MOVE operation individually calibrates both the qubit and coupler flux pulse amplitudes by making the MOVE insensitive to the relative phase of qubit and resonator, which signals a complete population transfer. As shown in the pulse schedule in Fig. S10(a), we first excite the qubit using an X_π gate and subsequently move this excitation to the computational resonator. We adjust the relative phase between qubit and resonator by applying an effective Z -rotation to the qubit by an angle φ . This is achieved by applying the following pulse sequence on the qubit: a $\pi/2$ -pulse around the y -axis, followed by a rotation around the x -axis by an angle φ , and another $\pi/2$ -pulse around the y -axis but rotating in the opposite direction. We repeat the sequence consisting of the MOVE operation and the Z -rotation $N - 1$ times, and apply a final MOVE operation before measuring the state of the qubit. The total number of moves, N , should be chosen to be an even number, such that most of the population is back in the qubit at the end of the experiment. If the MOVE operation does not fully transfer the state, the excited state probability measured at the end of the sequence oscillates as a function of the relative phase φ . This oscillation is due to the quantum interference of the state left in the qubit by the first MOVE with the part of the state that

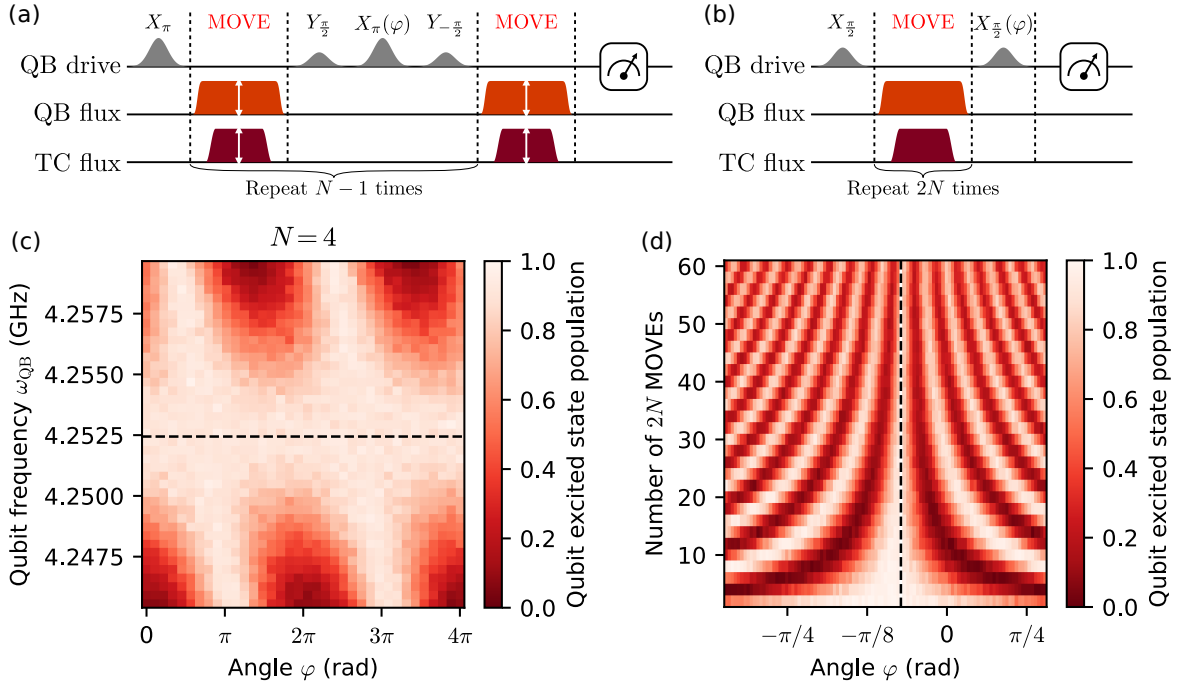


Figure S10. Calibration of the MOVE operation. (a), (b) Pulse schedules used for the fine calibration of the MOVE operating point and the calibration of the single-qubit phase correction of the MOVE, respectively. The schedules are described in detail in the supplementary text. (c) Experimental data showing the fine calibration measurement to optimise the flux pulse amplitude of the qubit Z-pulse, i.e., the diabatic qubit frequency ω_{QB} at the operation point of the MOVE. The optimal qubit frequency is visualized by the horizontal dashed line. (d) Experimental data for the calibration of the VZ phase correction. The optimal phase is visualized by the vertical dashed line.

has been moved to the computational resonator and back to the qubit. The more MOVE operations are applied in the fine calibration sequence, the more sensitive the resulting interference pattern is to a deviation from the optimal operating point. Experimental data are shown in Fig. S10(c) for a total number of $N = 4$ MOVE operations. For the data shown, we vary the amplitude of the qubit flux pulse and convert this voltage into the qubit frequency using the measured qubit flux dispersion. We take the average along the relative phase φ , and fit a parabola to the resulting data to find the optimal qubit frequency where the average qubit excited state probability is maximal. We perform a similar measurement (not shown here) to optimize the amplitude of the coupler flux pulse, keeping the qubit flux pulse amplitude the same.

Next, we determine the optimal virtual Z (VZ) phase for the MOVE qubit, which corrects for the single-qubit phase that is accumulated during the MOVE operation. Since we cannot directly probe the phase of a state in the computational resonator, we apply the MOVE operation in pairs and thus calibrate the common phase [S37], i.e., the phase obtained when moving an excitation from the qubit to the resonator and back. To achieve this, we consider the pulse schedule shown in Fig. S10(b). First, an equal superposition state is prepared in the qubit by applying an $X_{\pi/2}$ -pulse. Next, we move this superposition state back and forth between the qubit and the resonator, amplifying the accumulated single-qubit phase. Finally, we apply another $X_{\pi/2}$ -pulse with the rotation axis defined by φ in order to map the azimuthal angle of the qubit state to an excited state probability. If the phase of the qubit state was not changed by the application of the MOVE operations, we expect an excited state probability of 1. In Fig. S10(d), we show experimental data, where we vary the rotation axis of the second $\pi/2$ -pulse, φ , for an even number of MOVE operations. We average the data along the number of MOVE operations to extract the VZ phase correction. For demonstration purposes, we show the phase landscape for up to 60 MOVE operations, while for the benchmarking data we typically average over $2N = 2, 4, \dots, 10$ MOVE operations only.

2. Calibration of the CZ Gate

The initial calibration of the CZ gate is presented in the main text, therefore only the fine optimization of the operating point, including the measurement of the conditional phase and the population exchange, as well as the

calibration of the single-qubit phase corrections of the CZ gate are discussed here. We refine the calibration of the CZ gate by iteratively optimizing the qubit and coupler flux pulse parameters based on the measurement of the conditional phase and the population exchange, respectively. We start by optimizing the coupler frequency during the gate using the sequence shown in Fig. S11(a). To prepare the $|eg1\rangle$ state, we excite both the MOVE and CZ qubit with a X_π pulse and transfer the state of the MOVE qubit to the computational resonator. Next, we initiate the $|eg1\rangle \rightarrow |fg0\rangle \rightarrow |eg1\rangle$ population oscillations by applying flux pulses to the CZ qubit and the coupler connecting the CZ qubit and the computational resonator. Finally, we move the population of the computational resonator back to the MOVE qubit and apply X_π pulses to the MOVE and CZ qubit to de-excite them to the ground state, assuming the CZ gate performed a full population oscillation. We extract the operating point of the CZ gate from the minimum in the excited state probability of the MOVE qubit. The excited state probability of the CZ qubit also reveals the population oscillations, however, in general we obtain higher signal-to-noise for the MOVE qubit, as the readout is optimized to distinguish the qubit states $|g\rangle$ and $|e\rangle$, whereas the CZ qubit oscillates between $|g\rangle$ and $|f\rangle$. When varying the flux pulse amplitudes of both the CZ qubit and coupler pulses, we obtain the two-dimensional population landscape shown in Fig. S11(c). We use the qubit and coupler flux dispersions to express the flux pulse amplitudes in terms of the respective component frequency during the gate. We obtain the optimal coupler frequency by fitting the excited state probability of the MOVE qubit for a one-dimensional subset of the data as shown in Fig. S11(e).

Next, we optimize the qubit frequency during the CZ gate based on the measurement of the conditional phase. The pulse schedule used for measuring the phase accumulation of the CZ qubit depending on the state of the computational resonator is shown in Fig. S11(b). The CZ qubit is prepared in a superposition state by applying an $X_{\frac{\pi}{2}}$ -pulse to enable the measurement of the phase accumulation. The state of the computational resonator during the CZ gate depends on whether we apply the initial X_π -pulse on the MOVE qubit before moving the qubit state to the resonator. After the first MOVE operation, we apply flux pulses to the CZ qubit and the coupler connecting the CZ qubit and the computational resonator to implement the CZ gate. Finally, we apply an additional $\frac{\pi}{2}$ -pulse on the CZ qubit with rotation axis φ to map the azimuthal angle of the qubit state to the Z -basis, i.e., to an excited state probability. From the measurement of the excited state probability versus the angle φ , we determine the single-qubit phase accumulation of the CZ qubit for the two cases where the resonator is in the ground state or the first excited state. Fig. S11(d) shows the measurement of the conditional phase when sweeping the frequencies during gate operation of both the CZ qubit and its tunable coupler. We obtain the optimal qubit frequency during the CZ gate from a fit to a one-dimensional subset of the data with fixed coupler frequency at the point where the conditional phase is equal to π as shown in Fig. S11(f).

Next, we discuss the calibration of the single-qubit phase corrections of the CZ gate for both the computational resonator and the CZ qubit using the circuits shown in Fig. S12(a) and (b), respectively. First, we prepare an equal superposition state in the target qubit by applying an $X_{\frac{\pi}{2}}$ -pulse. The target qubit can be either the MOVE qubit or the CZ qubit. Before applying the CZ gate N times between the computational resonator and the CZ qubit, we move the population of the MOVE qubit to the resonator. Finally, we apply another MOVE operation followed by a $X_{\frac{\pi}{2}}$ -pulse in order to map the azimuthal angle of the qubit state to an excited state probability. If the phase of the target qubit has not been changed by applying the CZ gates, we expect the excited state probability to be equal to 1. We note that we apply the MOVE operations in the circuit shown in Fig. S12(b) even though there is no population in the MOVE qubit, because the flux pulses that implement a MOVE operation between the MOVE qubit and the computational resonator can affect the single-qubit phase accumulation of the CZ qubit due to flux cross-talk. Experiment data of the calibration of the single-qubit phase corrections for the CZ gate are shown in Fig. S12(c) and (d). If the CZ qubit is the target qubit, the phase accumulation that we measure originates purely from the frequency change of the CZ qubit during the CZ gate (ignoring flux cross-talk). However, if the MOVE qubit is the target qubit, the total accumulated phase between the $\frac{\pi}{2}$ -pulses generally contains different contributions. To measure the pure single-qubit phase accumulation of the computational resonator due to the dynamic frequency tuning during the CZ gate, we ensure that the previously calibrated VZ correction of the MOVE operation, VZ_{MOVE} , is applied. Furthermore, we account for the time-dependent phase due to the relative rotation of the rotating frames of the MOVE qubit and the computational resonator by adding a phase, $\Delta \cdot N \cdot t_{\text{CZ}} = (\omega_{\text{QB}} - \omega_{\text{CR}}) \cdot N \cdot t_{\text{CZ}}$, which is proportional to the detuning of the MOVE qubit and the resonator, as well as to the total time in between the MOVE operations, $N \cdot t_{\text{CZ}}$.

3. Characterization of the Computational Resonator

We characterize the frequency and coherence properties of the computational resonator by employing the MOVE operation to (de)populate the resonator. The circuit to measure the relaxation time is shown in Fig. S13(a): we excite one of the qubits using an X_π -pulse. After moving the excitation to the resonator, it will decay according to the resonator relaxation rate. After a variable delay time, we use a second MOVE operation to move the state back and

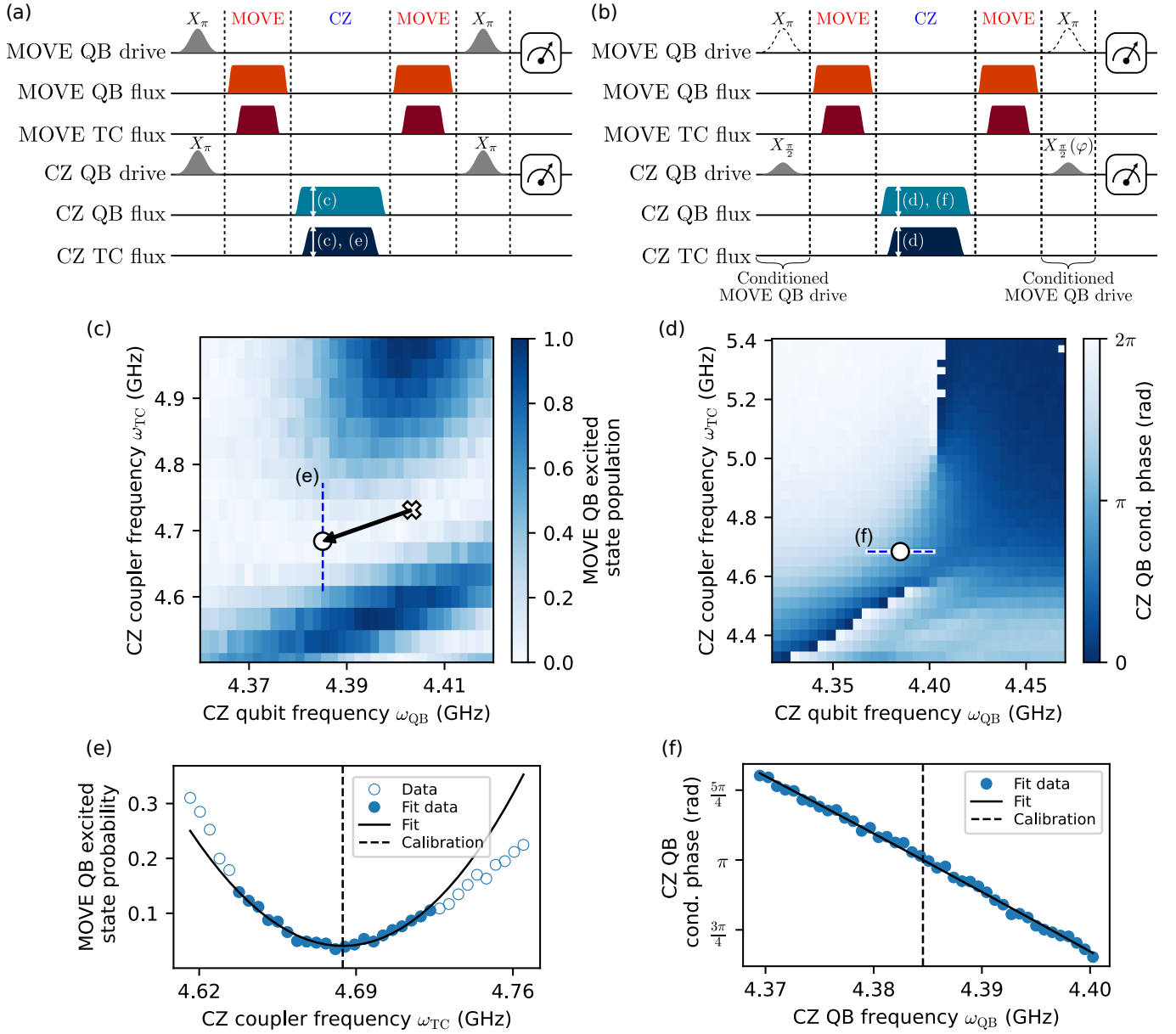


Figure S11. Calibration of the CZ gate. (a), (b) Pulse schedules to calibrate the population exchange and conditional phase, respectively. The flux pulses implementing the CZ gate to be calibrated are annotated with the measurement data figures, for which the respective pulse amplitude is varied. (c), (d) Experimental data showing the population exchange and conditional phase measured as a function of both the qubit and coupler frequencies realized during the gate operation by varying the respective flux pulse amplitudes. The blue dashed lines indicate the sweep ranges used for the one-dimensional data shown in (e) and (f), respectively. The white markers represent the operating point of the CZ gate inferred from the initial calibration discussed in the main text (cross) and the final calibration after several iterations of optimizing the flux pulse parameters based on the measurement of the population exchange and the conditional phase (circle). (e) Experimental data of the excited state probability of the MOVE qubit versus the coupler frequency during the gate. We approximate the minimum in the excited state probability with a quadratic fit (black solid line) that is applied to a subset of the data points (blue solid circles) obtained by removing data points from either side based on the R-squared value of the fit. (f) Experimental data of the conditional phase versus the qubit frequency during the gate. The optimal operating point of the CZ gate is indicated by the black dashed lines in (e) and (f).

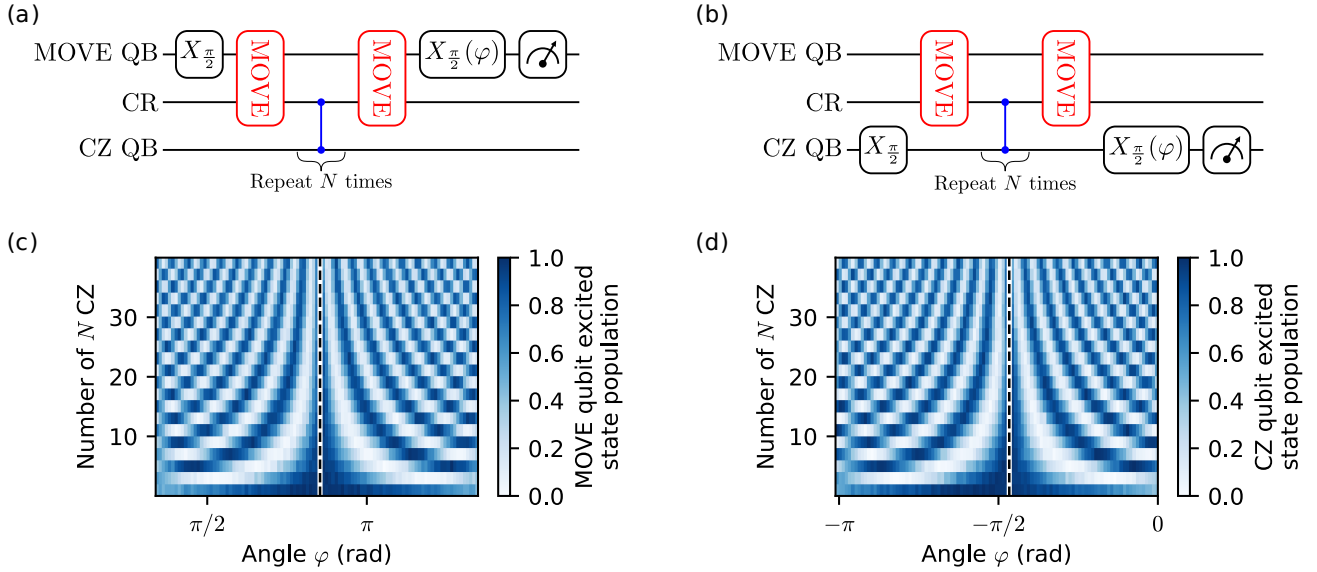


Figure S12. Calibration of the single-qubit phase corrections for the CZ gate. (a), (b) Pulse schedules to extract the single-qubit phase corrections of the computational resonator and the CZ qubit, respectively. (c), (d) Experiment data of the excited state probability of the qubit with the Ramsey sequence corresponding to the circuits shown in (a) and (b). We vary the angle φ and the total number of CZ gates N to obtain the optimal phase corrections. Since the additional contributions (VZ_{MOVE} , $\Delta \cdot t_{\text{CZ}}$) have been accounted for during the execution of the experiment, the vertical black dashed lines directly represent the optimal VZ rotation angle.

measure the remaining population in the qubit. The data in Fig. S13(b) shows the exponential decay from which we extract the resonator relaxation time $T_1 = 5.53 \pm 0.32 \mu\text{s}$.

To measure the T_2^* coherence time of the resonator, we employ Ramsey interferometry as shown in Fig. S13(c). This measurement is based on a technique outlined in [S73]. We prepare a superposition state in the MOVE qubit by applying an $X_{\pi/2}$ -pulse and use the MOVE operation to transfer the prepared state into the resonator. After a certain delay time t , we use a subsequent MOVE operation to move the superposition back to the qubit. Finally, we apply an $X_{\pi/2}(\phi)$ -pulse on the qubit, whose rotation axis is advanced with respect to the X-axis by ϕ . The excited state probability of the qubit at the end of the circuit oscillates at the difference frequency of the qubit and the computational resonator, which can be quite large, i.e., on the order of 100 MHz. We use a virtual detuning Δ to advance the phase of the second $\pi/2$ pulse by $\phi = \Delta t$ to effectively slow down the oscillations in the excited state probability of the qubit, such that the observed oscillation frequency $\omega = \omega_{\text{QB}} - \omega_{\text{CR}} - \Delta$ is comparable to the inverse of the T_2^* time. Both the oscillation frequency ω and the dephasing time T_2^* , are extracted from an exponentially decaying sinusoidal fit. The measurement data in Fig. S13(d) shows the Ramsey fringes from which we extract $T_2^* = 10.9 \pm 1.0 \mu\text{s}$. By additionally sweeping the virtual detuning (Fig. S13(e)), we can measure the eigenfrequency of the computational resonator. The excited state probability of the qubit versus the delay time is Fourier transformed. In Fig. S13(f), we show the extracted dominant frequency component versus the virtual detuning. We fit a sawtooth model to extract the value of the detuning (indicated by the orange circle), which corresponds to the detuning of the qubit and the computational resonator, i.e., $\Delta = \omega_{\text{QB}} - \omega_{\text{CR}}$.

Appendix F: Coherence Limit

To estimate the coherence limit F_{cz}^{c} for the MOVE operation and for the CZ gate, we employ the weak dissipation result F^{c} , valid at absolute zero, from Ref. [S42]

$$F^{\text{c}} = 1 - \frac{d\tau}{2(d+1)} \sum_{k=1}^N \left(\gamma_1^{(k)} + \gamma_{\varphi}^{(k)} \right). \quad (\text{S1})$$

Here, N is the number of involved components, d is the Hilbert space dimension, τ the gate duration, and $\gamma_1^{(k)}$ ($\gamma_{\varphi}^{(k)}$) is the energy relaxation (dephasing) rate for component k . Equation (S1) is valid as long as we do not leave

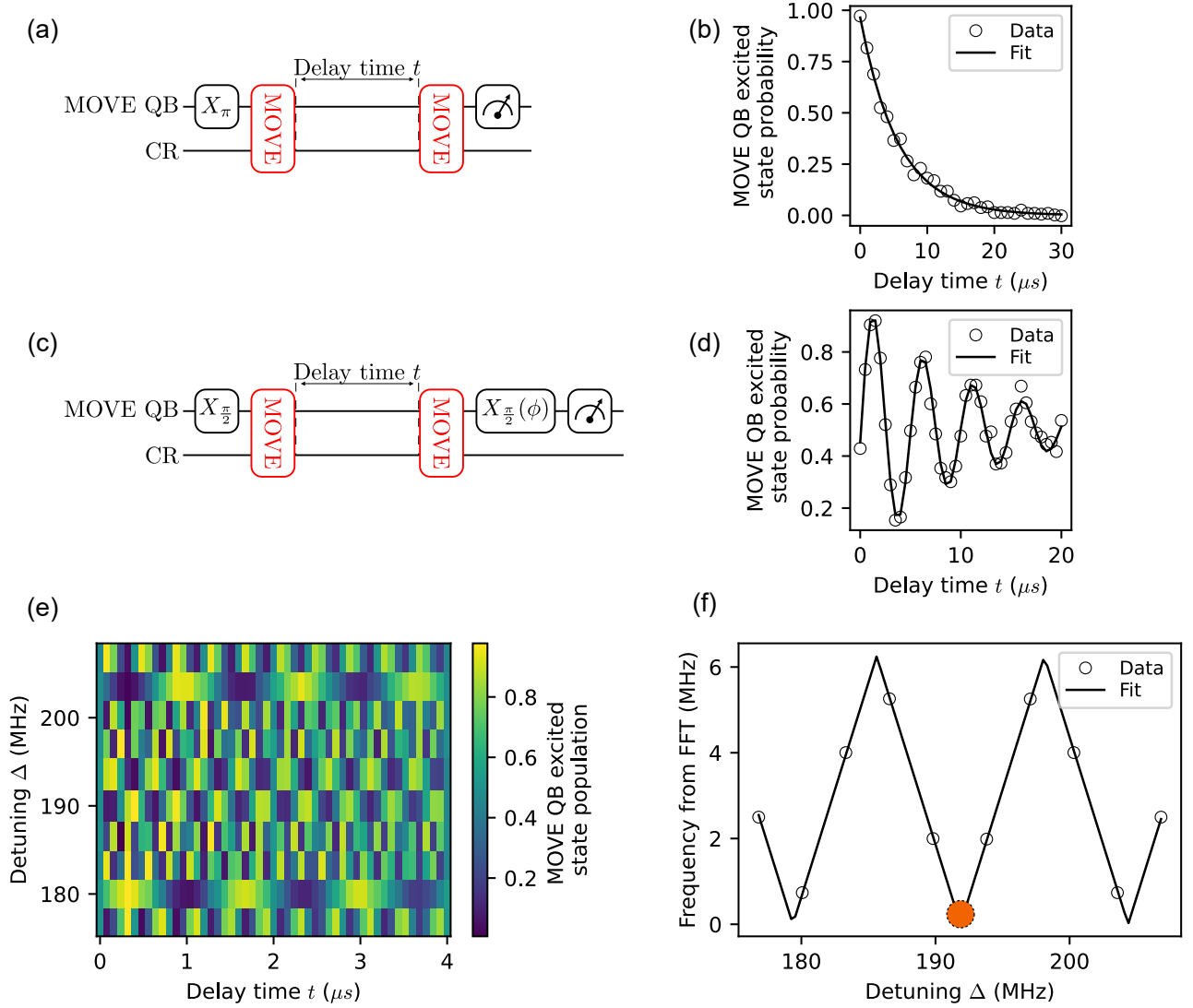


Figure S13. Characterization of the computational resonator. (a), (b) Circuit and corresponding experiment data to determine the relaxation time of the computational resonator T_1 . (c), (d) Circuit and measurement data from which the dephasing time of the resonator T_2^* is determined. (e) Experiment data with additional sweep over the virtual detuning Δ for the circuit shown in (c). (f) Fast Fourier transform of the qubit excited state probability versus delay time t shown in (e). We fit a sawtooth model to obtain the value of the virtual detuning corresponding to the frequency difference of the qubit and the computational resonator. The sweep range of the detuning is centered around the initial estimate for the qubit-resonator detuning obtained from a similar measurement but with much larger Nyquist frequency of approximately 250 MHz. Therefore, the qubit-resonator detuning (indicated by the orange circle) is obtained as the value of the detuning Δ that is closest to the center of the sweep range and where the Nyquist fit is equal to zero.

computational subspace during the operation. Furthermore, Eq. (S1) contains the implicit assumption that dephasing is caused by a white noise spectrum. In case of additional low frequency noise satisfying a $1/f$ noise spectral density, Eq. (S1) would contain an additional quadratic contribution for the dephasing rate. In the experiment, we verify that we are dominated by white noise since the envelope of our Ramsey curves decay exponentially and not Gaussian. We thus only consider the linear white noise contributions.

To use Eq. (S1) for the MOVE operation of duration τ_m , we treat it as an effective single-qubit gate and make the simple assumption that we assign half of the gate duration to qubit decoherence and half of the gate time to CR decay.

$$F_m^c = 1 - \frac{\tau_m}{6} (\gamma_1^q + \gamma_1^r + \gamma_\phi^q + \gamma_\phi^r),$$

where subscript q (r) refers to the MOVE qubit (CR). For the CZ gate, we leave the computational space and apply the formulation from Ref. [S43]

$$F_{cz}^c = 1 - \frac{1}{2}\tau_{cz}\gamma_1^q - \frac{3}{10}\tau_{cz}\gamma_1^r - \frac{61}{80}\tau_{cz}\gamma_\varphi^q - \frac{29}{80}\tau_{cz}\gamma_\varphi^r, \quad (S2)$$

where τ_{cz} is the CZ gate time. In the presence of a thermal qubit (CR) population of n_q (n_r) photons, the coherence limits reduces further by

$$F_m^c \rightarrow F_m^c - \frac{1}{3}\tau_m\gamma_1^q n_q - \frac{1}{3}\tau_m\gamma_1^r n_r, \quad F_{cz}^c \rightarrow F_{cz}^c - \frac{9}{5}\tau_{cz}\gamma_1^q n_q - \frac{7}{5}\tau_{cz}\gamma_1^r n_r. \quad (S3)$$

For the gate durations, we use the values from Tab.S4 and for the decay rates, we employ the values from Tab.S2. We neglect thermal effects since we are still in the saturation regime of Planck statistics for qubit temperatures below 50 mK [S74, S75]. The coherence limits given in the main text are the arithmetic mean of the fidelity limits of the individual qubits

We can also estimate the effect of decoherence on the GHZ state preparation. For this, we consider the transpiled circuit we employ for N -qubit GHZ state generation (cf. Fig 4(a)), which can be schematically written as

$$\underbrace{Y_{\frac{\pi}{2}}}_{(1)} + \underbrace{\text{MOVE}}_{(2)} + \underbrace{\text{CZ}}_{(3)} + \underbrace{\text{MOVE}}_{(4)} + \underbrace{Y_{\frac{\pi}{2}} + X_\pi}_{(5)}. \quad (S4)$$

Step (1) corresponds to a $\pi/2$ -rotation about the y -axis which is applied to all N qubits. In step (2), we employ a MOVE operation between a dedicated MOVE qubit and the CR. Step (3) corresponds to a cascade of $(N - 1)$ CZ operations, followed by a MOVE operation in (4) which swaps the CR state back to the MOVE qubit. Finally, we apply a $\pi/2$ -rotation about the y -axis and a π -rotation about the x -axis to each of the CZ qubits. In case F_i corresponds to the coherence-limited fidelity of step (i), we approximate the coherence limit of the entire circuit by assuming

$$F_{\text{GHZ}} = F_1 F_2 F_3 F_4 F_5. \quad (S5)$$

The individual fidelity contributions are estimated by

$$F_1 = \prod_k F_s^{(k)}, \quad F_2 = F_4 = F_m \prod_{k \neq m} F_{i,m}^{(k)}, \quad F_3 = \prod_{k \neq m} F_{cz}^{(k)} \left(F_{i,cz}^{(k)} \right)^{N-2}, \quad F_5 = \prod_{k \neq m} (F_s^{(k)})^2 (F_{i,s}^{(m)})^2. \quad (S6)$$

Here, $F_s^{(k)}$ denotes the single-qubit gate fidelity coherence limit for qubit k , given by [S42]

$$F_s^{(k)} = 1 - \frac{\tau_s}{3} \left(\gamma_1^{(k)} + \gamma_\varphi^{(k)} \right) - \frac{2}{3} n_q^{(k)} \gamma_1^{(k)}.$$

F_m corresponds to the MOVE operation coherence limit and $F_{i,m}^{(k)}$ corresponds to the fidelity limit for qubit k which idles during the MOVE operation. The quantity $F_{cz}^{(k)}$ corresponds to the fidelity limit for the CZ gate between the CR and qubit k and $F_{i,cz}^{(k)}$ denotes the idling fidelity of qubit k in case there is no CZ gate applied during the CZ gate cascade. The exponent $N - 2$ results from the fact that there is one CZ gate per qubit applied and each qubit idles during the remaining $(N - 2)$ CZ gates. Finally, $F_{i,s}^{(m)}$ is the idling fidelity limit for the MOVE qubit during the final two single-qubit gates. For simplicity, we dropped the superscript c for the coherence limits

We exploit the fact that the coherence limit is in first order independent of the applied gate. Therefore, we approximate the idling fidelities by the measured single-qubit gate fidelities. Thus, $F_{i,s} = F_s$ and $F_{i,s}^{(m)}$ as well as $F_{i,cz}^{(k)}$ are treated like an effective single-qubit gate with the same gate time as the respective qubit-resonator operation. As a consequence, Eq. (S5) can be expressed as

$$F_{\text{GHZ}} = F_m^2 F_s^{(m)} \left(F_{i,s}^{(m)} \right)^2 \prod_{k \neq m} \left(F_s^{(k)} \right)^3 \left(F_{i,m}^{(k)} \right)^2 \left(F_{i,cz}^{(k)} \right)^{N-2} F_{cz}^{(k)}. \quad (S7)$$

As for the coherence limit estimation for the individual gates, hybridization effects with tunable couplers are neglected. However, we take the finite temperature into account this time, since even for a qubit temperature of 40 mK, finite temperature effects accumulate due to the large amount of gates in the circuit. Since we cannot directly measure the CR temperature, we perform a work case estimation and assume its temperature to coincide with the hottest qubit in

Tab. S2, $T_r = 46.3$ mK. For the six qubit GHZ state, we then find a fidelity limit of $F_{\text{GHZ}} \simeq 0.910$. After multiplying with the readout fidelities, this limit reduces to 0.842. As a comparison, we measured a GHZ fidelity of 0.815 without REM and 0.860 with REM. Although the model Eq. (S7) is relatively simple, we conclude that the main effect of GHZ infidelity results from decoherence.

We particularly observe that the resonator life time is significantly shorter than the life time of the qubits. Since the resonator is involved in all qubit-resonator operations, this low life time is expected to set a dominant limitation on the GHZ state fidelity. For that, we employ the approximation that the qubits and the computational resonator are T_1 limited and drop all dephasing terms (for the resonator, this is a very accurate assumption). Simultaneously, we assume that the qubit-resonator operations add significantly more infidelity than the single-qubit gates, implying that we treat all single-qubit gates as ideal. We furthermore assume a temperature of absolute zero and, for simplicity, equal duration τ of CZ gate and MOVE operation, implying $F_{i,m}^{(k)} = F_{i,cz}^{(k)}$. With these rough approximations, we have

$$F_{\text{GHZ}} \simeq \prod_{k \neq m} \left(F_{i,cz}^{(k)} \right)^N F_{cz}^{(k)} = \prod_{k \neq m} \left(1 - \frac{\tau}{3} \gamma_1^{(k)} \right)^N \left(1 - \frac{\tau}{2} \gamma_1^{(k)} - \frac{3}{10} \gamma_1^r \right). \quad (\text{S8})$$

In the limit $N \gg 1$, $\gamma_1^{(k)} \tau \ll 1$, $\gamma_1^r \tau \ll 1$, we can further approximate by

$$F_{\text{GHZ}} \simeq \prod_{k \neq m} e^{-N \frac{\tau}{3} \gamma_1^{(k)}} \prod_{k \neq m} e^{-\frac{\tau}{2} \gamma_1^{(k)} - \frac{3\tau}{10} \gamma_1^r} = e^{-\tau \left(\frac{N}{3} + \frac{1}{2} \right) \sum_{k \neq m} \gamma_1^{(k)}} e^{-(N-1) \frac{3\tau}{10} \gamma_1^r}, \quad (\text{S9})$$

where we use an exponential approximation, analogous as has been used for the derivation of the Porter-Thomas distribution in Ref. [S76]. With this approximation, F_{GHZ} decouples into a qubit and a resonator decay term

$$F_{\text{GHZ}} \simeq \underbrace{e^{-\tau \left(\frac{N}{3} + \frac{1}{2} \right) (N-1) \bar{\gamma}_1^q}}_{\text{Qubit tail}} \cdot \underbrace{e^{-(N-1) \frac{3\tau}{10} \gamma_1^r}}_{\text{Resonator tail}}, \quad (\text{S10})$$

where $\bar{\gamma}_1^q$ is the mean energy decay rate of the involved CZ qubits. By comparing the decay constants, the constraint that the resonator life time limits the GHZ fidelity is then given by

$$\gamma_1^r \gg \left(\frac{10N}{9} + \frac{5}{3} \right) \bar{\gamma}_1^q. \quad (\text{S11})$$

For our six qubit QPU, this implies $\gamma_1^r \gg 8.3 \bar{\gamma}_1^q$. For our QPU, we have $\gamma_1^r \simeq 6.7 \bar{\gamma}_1^q$, implying that this condition is not met. As such, the CR decoherence is expected to have a significant effect on the GHZ coherence limit, but the dominating error contribution is the depolarization of the qubits during idling gates. In fact, setting $\gamma_1^r = 0$ in Eq. (S7) raises F_{GHZ} from 0.842 to 0.867 (taking finite readout fidelity into account). Equation (S11) also implies that for $N \gg 1$, it can be beneficial to use the qubit with the lowest life time as MOVE qubit since during the long CZ cascade, it always idles in the ground state and does not contribute to $\bar{\gamma}_1^q$.

Appendix G: Jaynes-Cummings gate

1. Time evolution in the rotating frame

Let us consider here the dynamics of a quantum state $|\psi\rangle$, governed by the time-dependent Hamiltonian $\hat{H}(t) = \hat{H}_0 + \hat{V}(t)$. Here, we have separated the full Hamiltonian into a time-independent part \hat{H}_0 , and into an interaction part $\hat{V}(t)$ which can be time dependent. In general, \hat{H}_0 and $\hat{V}(t)$ do not commute.

Let us make a transformation into an interaction picture using the unitary operator $\hat{R}(t) = e^{i\hat{H}_0 t/\hbar}$. Consequently, the state vector is transformed as

$$|\psi\rangle' = \hat{R} |\psi\rangle \quad (\text{S1})$$

The Schrödinger equation defines the time evolution in the lab frame according to:

$$i\hbar \partial_t |\psi\rangle = \hat{H} |\psi\rangle \quad (\text{S2})$$

We can derive a similar equation defining the time evolution in the rotating frame:

$$\begin{aligned}
i\hbar\partial_t\hat{R}^\dagger(t)|\psi\rangle' &= (\hat{H}_0 + \hat{V})\hat{R}^\dagger(t)|\psi\rangle' \\
\hat{H}_0\hat{R}^\dagger(t)|\psi\rangle' + i\hbar\hat{R}^\dagger(t)\partial_t|\psi\rangle' &= (\hat{H}_0 + \hat{V})\hat{R}^\dagger(t)|\psi\rangle' \\
i\hbar\hat{R}^\dagger(t)\partial_t|\psi\rangle' &= \hat{V}\hat{R}^\dagger(t)|\psi\rangle' \\
i\hbar\partial_t|\psi\rangle' &= \hat{R}(t)\hat{V}\hat{R}^\dagger(t)|\psi\rangle'.
\end{aligned} \tag{S3}$$

Therefore, the Hamiltonian in the rotating frame is given by:

$$\hat{H}' = \hat{R}(t)\hat{V}\hat{R}^\dagger(t). \tag{S4}$$

Next, we want to relate the time evolution operators in the two frames to each other.

$$\begin{aligned}
i\hbar\partial_t|\psi\rangle'(t) &= \hat{R}(t)\hat{V}\hat{R}^\dagger(t)|\psi\rangle'(t) \\
i\hbar\partial_t\hat{U}'(t, t_0)|\psi\rangle'(t_0) &= \hat{R}(t)\hat{V}\hat{R}^\dagger(t)\hat{U}'(t, t_0)|\psi\rangle'(t_0) \\
i\hbar\partial_t\hat{U}'(t, t_0) &= \hat{R}(t)\hat{V}\hat{R}^\dagger(t)\hat{U}'(t, t_0).
\end{aligned} \tag{S5}$$

Next, we compare the result from the rotating frame, to the time evolution operator in the Schrödinger picture:

$$\begin{aligned}
i\hbar\partial_t|\psi\rangle(t) &= \hat{H}|\psi\rangle(t) \\
i\hbar\partial_t\hat{U}(t, t_0)|\psi\rangle(t_0) &= \hat{H}\hat{U}(t, t_0)|\psi\rangle(t_0) \\
i\hbar\partial_t\hat{U}(t, t_0) &= \hat{H}\hat{U}(t, t_0).
\end{aligned} \tag{S6}$$

The two time evolution operators can easily be transformed into one another:

$$\begin{aligned}
|\psi\rangle'(t) &= \hat{U}'(t, t_0)|\psi\rangle'(t_0) \\
\hat{R}(t)|\psi\rangle(t) &= \hat{U}'(t, t_0)\hat{R}(t_0)|\psi\rangle(t_0) \\
\hat{R}(t)\hat{U}(t, t_0)|\psi\rangle(t_0) &= \hat{U}'(t, t_0)\hat{R}(t_0)|\psi\rangle(t_0) \\
\hat{R}(t)\hat{U}(t, t_0)\hat{R}^\dagger(t_0) &= \hat{U}'(t, t_0).
\end{aligned} \tag{S7}$$

2. Jaynes Cummings Hamiltonian

The Rabi Hamiltonian describes the time evolution of a two-level system, i.e., a qubit, interacting with a bosonic mode, here called a computational resonator. In the lab frame and ignoring the zero-point energy of the computational resonator, the Hamiltonian is given by

$$\hat{H} = \hat{H}_{\text{resonator}} + \hat{H}_{\text{qubit}} + \hat{H}_{\text{interaction}} = \hbar\omega_r\hat{a}^\dagger\hat{a} + \hbar\omega_q\frac{\hat{\sigma}_z}{2} + \frac{\hbar\Omega}{2}(\hat{\sigma}^+ + \hat{\sigma}^-)(\hat{a} + \hat{a}^\dagger), \tag{S8}$$

Using Eq. S4 we can transform the Hamiltonian from the Schrödinger picture (lab frame) to the interaction picture (computational frame), which is defined by the choice of rotating frame, $\hat{H}_0 = \hat{H}_{\text{resonator}} + \hat{H}_{\text{qubit}}$

$$\hat{H}_{\text{comp}} = \frac{\hbar\Omega}{2}e^{i\hat{H}_0t/\hbar}(\hat{a}\hat{\sigma}^- + \hat{a}^\dagger\hat{\sigma}^+ + \hat{a}\hat{\sigma}^+ + \hat{a}^\dagger\hat{\sigma}^-)e^{-i\hat{H}_0t/\hbar} \tag{S9}$$

Using the Baker-Campbell-Hausdorff lemma ($e^X Y e^{-X} = Y + [X, Y] + 1/2![X, [X, Y]] + \dots + 1/n![X, [X, \dots[X, Y]\dots]]$) and the commutation relations $[\hat{a}^\dagger\hat{a}, \hat{a}] = -\hat{a}$, $[\hat{a}^\dagger\hat{a}, \hat{a}^\dagger] = \hat{a}^\dagger$, and $[\hat{\sigma}_z, \hat{\sigma}^\pm] = \pm 2\hat{\sigma}^\pm$, we have

$$\hat{H}_{\text{comp}} = \frac{\hbar\Omega}{2} \left(\hat{a}\hat{\sigma}^- e^{-i(\omega_r + \omega_q)t} + \hat{a}^\dagger\hat{\sigma}^+ e^{i(\omega_r + \omega_q)t} + \hat{a}\hat{\sigma}^+ e^{-i(\omega_r - \omega_q)t} + \hat{a}^\dagger\hat{\sigma}^- e^{i(\omega_r - \omega_q)t} \right). \tag{S10}$$

According to the rotating wave approximation (RWA), the two quickly oscillating terms may be ignored. In this case, we end up with the Jaynes-Cummings Hamiltonian in the interaction picture:

$$\hat{H} = \hat{H}_0 + \frac{\hbar\Omega}{2} (\hat{a}^\dagger\hat{\sigma}^- + \hat{a}\hat{\sigma}^+). \tag{S11}$$

According to the Jaynes-Cummings Hamiltonian in Eq. S11, where non-excitation-conserving transitions have been dropped by applying the RWA, we only have to consider excitation-conserving transitions between the qubit-resonator states $|r, q\rangle$:

$$|n, g\rangle \leftrightarrow |n-1, e\rangle, \quad (\text{S12})$$

where n is the total number of excitations of the qubit-resonator state and the eigenvalue of the operator $\hat{N} = |e\rangle\langle e| + \hat{a}^\dagger\hat{a}$. This operator commutes with the interaction term in the Hamiltonian:

$$\begin{aligned} [\hat{H}_{\text{int}}, \hat{N}] &= \frac{\hbar\Omega}{2} (\hat{a}^\dagger[\hat{\sigma}^-, |e\rangle\langle e|] + [\hat{a}^\dagger, \hat{a}^\dagger\hat{a}]\hat{\sigma}^- + \hat{a}[\hat{\sigma}^+, |e\rangle\langle e|] + [\hat{a}, \hat{a}^\dagger\hat{a}]\hat{\sigma}^+) \\ &= \frac{\hbar\Omega}{2} (\hat{a}^\dagger\hat{\sigma}^- - \hat{a}^\dagger\hat{\sigma}^- - \hat{a}\hat{\sigma}^+ + \hat{a}\hat{\sigma}^+) = 0. \end{aligned} \quad (\text{S13})$$

Using the eigenstates of \hat{N} as a basis, the Hamiltonian can be represented by a block diagonal matrix:

$$\hat{H} = \begin{bmatrix} 1 & 0 & 0 & 0 & \dots & \dots & \dots \\ 0 & \hat{H}_1 & 0 & 0 & \ddots & \ddots & \ddots \\ 0 & 0 & \hat{H}_2 & 0 & \ddots & \ddots & \ddots \\ \vdots & \ddots & \ddots & \ddots & \ddots & \ddots & \ddots \\ \vdots & \ddots & \ddots & 0 & \hat{H}_n & 0 & \ddots \\ \vdots & \ddots & \ddots & \ddots & \ddots & \ddots & \ddots \end{bmatrix} \quad (\text{S14})$$

The (2×2) matrices representing the manifolds with equal number of excitations n , are given by

$$\hat{H}_n = \begin{pmatrix} \langle n-1, e | \hat{H} | n-1, e \rangle & \langle n-1, e | \hat{H} | n, g \rangle \\ \langle n, g | \hat{H} | n-1, e \rangle & \langle n, g | \hat{H} | n, g \rangle \end{pmatrix} = \hbar \begin{pmatrix} \omega_r(n-1) + \frac{\omega_q}{2} & \frac{\Omega\sqrt{n}}{2} \\ \frac{\Omega\sqrt{n}}{2} & n\omega_r - \frac{\omega_q}{2} \end{pmatrix} \quad (\text{S15})$$

When reintroducing the zero-point energy of the computational resonator ($+\hat{I}\hbar\omega_r/2$) in \hat{H}_n and defining $\Delta = \omega_r - \omega_q$, we can rewrite the elements in the block-diagonal matrix as:

$$\hat{H}_n = \hbar \begin{pmatrix} n\omega_r - \frac{\Delta}{2} & \frac{\Omega\sqrt{n}}{2} \\ \frac{\Omega\sqrt{n}}{2} & n\omega_r + \frac{\Delta}{2} \end{pmatrix} = n\hbar\omega_r\hat{I} - \frac{\hbar\Delta}{2}\hat{\sigma}_z + \frac{\hbar\Omega\sqrt{n}}{2}\hat{\sigma}_x \quad (\text{S16})$$

The time evolution in the lab frame can be calculated by the propagator

$$\begin{aligned} U_{n,\text{lab}}(t, 0) &= e^{-i\hat{H}_n t/\hbar} \\ &= e^{-in\omega_r t} \begin{pmatrix} \cos\left(\frac{1}{2}\Omega(\Delta, n)t\right) + i\frac{\Delta\sin\left(\frac{1}{2}\Omega(\Delta, n)t\right)}{\Omega(\Delta, n)} & -i\frac{\Omega\sqrt{n}\sin\left(\frac{1}{2}\Omega(\Delta, n)t\right)}{\Omega(\Delta, n)} \\ -i\frac{\Omega\sqrt{n}\sin\left(\frac{1}{2}\Omega(\Delta, n)t\right)}{\Omega(\Delta, n)} & \cos\left(\frac{1}{2}\Omega(\Delta, n)t\right) - i\frac{\Delta\sin\left(\frac{1}{2}\Omega(\Delta, n)t\right)}{\Omega(\Delta, n)} \end{pmatrix} \end{aligned} \quad (\text{S17})$$

Here we have defined the photon number and detuning dependent generalised Rabi frequency $\Omega(\Delta, n) = \sqrt{\Delta^2 + n\Omega^2}$, which characterises the effective coupling between the states $|n-1, e\rangle$ and $|n, g\rangle$.

a. Free time evolution When the detuning between the qubit and the computational resonator is much larger than the Rabi frequency ($\sqrt{n}\Omega/\Delta \ll 1$), we can approximate $\Omega(\Delta, n) = \Delta\sqrt{1 + n\Omega^2/\Delta^2} \approx \Delta$. In this case, the unitary operator simplifies to the free time evolution:

$$U_{n,\text{lab}}(\sqrt{n}\Omega/\Delta \ll 1) \simeq e^{-in\omega_r t} \begin{pmatrix} e^{i\frac{\Delta}{2}t} & 0 \\ 0 & e^{-i\frac{\Delta}{2}t} \end{pmatrix} \quad (\text{S18})$$

b. Resonant population exchange To obtain a full population exchange between the states $|n-1, e\rangle$ and $|n, g\rangle$, the qubit and computational resonator have to be on resonance, i.e., $\Delta = 0$ during the MOVE operation. Therefore the time evolution in the lab frame simplifies to

$$U_{n,\text{lab}}(\Delta = 0) = e^{-in\omega_r t} \begin{pmatrix} \cos\left(\frac{1}{2}\sqrt{n}\Omega t\right) & -i\sin\left(\frac{1}{2}\sqrt{n}\Omega t\right) \\ -i\sin\left(\frac{1}{2}\sqrt{n}\Omega t\right) & \cos\left(\frac{1}{2}\sqrt{n}\Omega t\right) \end{pmatrix}, \quad (\text{S19})$$

where ω_g is the gate frequency, meaning the frequency of both the qubit and the computational resonator during the Jaynes-Cummings gate. The Jaynes-Cummings gate is calibrated to achieve a full population exchange in the single excitation manifold, $n = 1$. Assuming that Ω is constant during the gate, i.e., square flux pulse applied to the tunable coupler, the gate time follows as $t = \pi/\Omega$. By transforming from the lab frame to a rotating frame where both the qubit and the computational resonator are oscillating at ω_g (gate frame), i.e., $\hat{R}_g = e^{in\omega_g t \hat{I}}$, the time evolution for the lowest four excitation manifolds simplifies to

$$\begin{bmatrix} |0, g\rangle & |0, e\rangle & |1, g\rangle & |1, e\rangle & |2, g\rangle & |2, e\rangle & |3, g\rangle & |3, e\rangle & |4, g\rangle \\ \left[\begin{array}{cccccccccc} 1 & 0 & 0 & 0 & 0 & 0 & 0 & 0 & 0 \\ 0 & 0 & -i & 0 & 0 & 0 & 0 & 0 & 0 \\ 0 & -i & 0 & 0 & 0 & 0 & 0 & 0 & 0 \\ 0 & 0 & 0 & \cos\left(\frac{\sqrt{2}}{2}\pi\right) & -i\sin\left(\frac{\sqrt{2}}{2}\pi\right) & 0 & 0 & 0 & 0 \\ 0 & 0 & 0 & -i\sin\left(\frac{\sqrt{2}}{2}\pi\right) & \cos\left(\frac{\sqrt{2}}{2}\pi\right) & 0 & 0 & 0 & 0 \\ 0 & 0 & 0 & 0 & 0 & \cos\left(\frac{\sqrt{3}}{2}\pi\right) & -i\sin\left(\frac{\sqrt{3}}{2}\pi\right) & 0 & 0 \\ 0 & 0 & 0 & 0 & 0 & -i\sin\left(\frac{\sqrt{3}}{2}\pi\right) & \cos\left(\frac{\sqrt{3}}{2}\pi\right) & 0 & 0 \\ 0 & 0 & 0 & 0 & 0 & 0 & 0 & 0 & -1 \\ 0 & 0 & 0 & 0 & 0 & 0 & 0 & 0 & 0 \end{array} \right] \end{bmatrix} \quad (\text{S20})$$

In most cases, the rotating frame of choice is the so-called computational frame, where the free time evolution of all components is effectively fully compensated by the rotating frame, which means that the unitary transformation going from lab to the computational frame is constructed using $\hat{H}_0 = n\hbar\omega_r \hat{I} - \frac{\hbar\Delta}{2} \hat{\sigma}_z$:

$$\hat{R}_{\text{lab} \rightarrow \text{comp}} = e^{i(n\omega_r \hat{I} - \frac{\Delta}{2} \hat{\sigma}_z)t} = e^{in\omega_r t \hat{I}} e^{-i\frac{\Delta}{2} t \hat{\sigma}_z} \quad (\text{S21})$$

The Hamiltonian in the computational frame follows from Eq. (S4)

$$\hat{H}_{n,\text{comp}} = \hat{R}_{\text{lab} \rightarrow \text{comp}} \hat{V} \hat{R}_{\text{lab} \rightarrow \text{comp}}^\dagger = \frac{\hbar\Omega\sqrt{n}}{2} e^{-i\frac{\Delta}{2} t \hat{\sigma}_z} \hat{\sigma}_x e^{i\frac{\Delta}{2} t \hat{\sigma}_z} = \frac{\hbar\Omega\sqrt{n}}{2} \begin{pmatrix} 0 & e^{-i\Delta t} \\ e^{i\Delta t} & 0 \end{pmatrix} \quad (\text{S22})$$

The time evolution in the computational frame can be calculated using Eqs. (S19), (S21) and (S7):

$$\begin{aligned} U_{n,\text{comp}}(t, t_0) &= \hat{R}_{\text{lab} \rightarrow \text{comp}} U_{n,\text{lab}}(t, t_0) \hat{R}_{\text{lab} \rightarrow \text{comp}}^\dagger \\ &= e^{in(\omega_r - \omega_g)(t-t_0)} \begin{pmatrix} e^{-i\frac{\Delta}{2}(t-t_0)} \cos\left(\frac{\sqrt{n}\Omega}{2}(t-t_0)\right) & -ie^{-i\Delta\frac{t+t_0}{2}} \sin\left(\frac{\sqrt{n}\Omega}{2}(t-t_0)\right) \\ -ie^{i\Delta\frac{t+t_0}{2}} \sin\left(\frac{\sqrt{n}\Omega}{2}(t-t_0)\right) & e^{i\frac{\Delta}{2}(t-t_0)} \cos\left(\frac{\sqrt{n}\Omega}{2}(t-t_0)\right) \end{pmatrix} \end{aligned} \quad (\text{S23})$$

In the computational frame we see that the frame tracking need to take into account all the times when a Jaynes-Cummings gate is applied. Assuming the Jaynes-Cummings gate to be instantaneous ($t = t_0$) and calibrated to obtain a full population exchange in the one-excitation manifold, the time evolution operator simplifies to:

$$U_{n,\text{comp}}(t = t_0, t_0) = \begin{pmatrix} \cos\left(\frac{\sqrt{n}\pi}{2}\right) & -ie^{-i\Delta t} \sin\left(\frac{\sqrt{n}\pi}{2}\right) \\ -ie^{i\Delta t} \sin\left(\frac{\sqrt{n}\pi}{2}\right) & \cos\left(\frac{\sqrt{n}\pi}{2}\right) \end{pmatrix} \quad (\text{S24})$$

Next, we derive the expected qubit probability for the populated Ramsey experiment demonstrated in the main text. We change to obtained when changing to the reference frame defined by $\hat{H}_{\text{ref}} = \hbar\omega_q(\hat{a}^\dagger \hat{a} + \frac{\hat{\sigma}_z}{2})$. As we will see below, in this frame the time evolution adds phase factors proportional to the detuning Δ and the number of excitations in the resonator. Therefore when sweeping the wait time we will observe two frequency components in the excited state probability of the second move qubit, one at $f_1 = \Delta$ and another one at $f_2 = 2\Delta$, corresponding to one and two photons in the resonator, respectively. To transform the Hamiltonian into the this frame, we use the following unitary:

$$\hat{R}_1 = e^{i\omega_q t (a^\dagger a \hat{I} + \frac{\hat{\sigma}_z}{2})} = e^{in\omega_q t \hat{I}} e^{i\frac{\omega_q}{2} t \hat{\sigma}_z} = e^{-i\frac{\omega_q}{2} t} e^{in\omega_q t} \begin{pmatrix} e^{i\omega_q t} & 0 \\ 0 & 1 \end{pmatrix}. \quad (\text{S25})$$

The first exponential creates a global phase and thus can be neglected. The second exponential adds an excitation-dependent phase to the corresponding state, while the matrix adds a qubit-state dependent phase. Using the considered reference frame Hamiltonian, the Jaynes-Cummings hamiltonian can be rewritten as:

$$\begin{aligned}
\hat{H} &= \hbar\omega_r \hat{a}^\dagger \hat{a} + \hbar\omega_q \frac{\hat{\sigma}_z}{2} + \frac{\hbar\Omega}{2} (\hat{a}^\dagger \hat{\sigma}^- + \hat{a} \hat{\sigma}^+) \\
&= \hbar\omega_q \hat{a}^\dagger \hat{a} + \hbar\omega_q \frac{\hat{\sigma}_z}{2} + \hbar(\omega_r - \omega_q) \hat{a}^\dagger \hat{a} + \frac{\hbar\Omega}{2} (\hat{a}^\dagger \hat{\sigma}^- + \hat{a} \hat{\sigma}^+) \\
&= \hat{H}_{\text{ref}} + \hbar\Delta \hat{a}^\dagger \hat{a} + \frac{\hbar\Omega}{2} (\hat{a}^\dagger \hat{\sigma}^- + \hat{a} \hat{\sigma}^+)
\end{aligned} \tag{S26}$$

By applying Eq S25, the interaction Hamiltonian becomes:

$$\begin{aligned}
\hat{H}_{\text{int}} &= e^{in\omega_q t} \begin{pmatrix} e^{i\omega_q t} & 0 \\ 0 & 1 \end{pmatrix} \left(\hat{H}_{\text{ref}} + \hbar\Delta \hat{a}^\dagger \hat{a} + \frac{\hbar\Omega}{2} (\hat{a}^\dagger \hat{\sigma}^- + \hat{a} \hat{\sigma}^+) \right) e^{-in\omega_q t} \begin{pmatrix} e^{-i\omega_q t} & 0 \\ 0 & 1 \end{pmatrix} - \hat{H}_{\text{ref}} \\
&= \hbar\Delta \hat{a}^\dagger \hat{a} + \frac{\hbar\Omega}{2} (\hat{a}^\dagger \hat{\sigma}^- e^{-i\omega_q t} + \hat{a} \hat{\sigma}^+ e^{i\omega_q t}) \\
&= \hbar \begin{pmatrix} (n-1)\Delta & \frac{\Omega\sqrt{n}}{2} e^{i\omega_q t} \\ \frac{\Omega\sqrt{n}}{2} e^{-i\omega_q t} & n\Delta \end{pmatrix} \\
&= \hbar n \Delta \hat{I} - \frac{\hbar\Delta}{2} \hat{\sigma}_z + \frac{\hbar\Omega\sqrt{n}}{2} (\cos(\omega_q t) \hat{\sigma}_x - \sin(\omega_q t) \hat{\sigma}_y) - \frac{\hbar\Delta}{2} \hat{I}
\end{aligned} \tag{S27}$$

We invoked the matrix representation of the Hamiltonian for a given excitation manifold n and neglect the constant offset term which doesn't contribute to the dynamics of the system. The unitary operator in this frame becomes:

$$\begin{aligned}
e^{-i\hat{H}_{\text{int}}t/\hbar} &= e^{-itn\Delta} e^{-i\frac{\Omega_{\text{eff}}t}{2} \left(\frac{\Omega\sqrt{n}}{\Omega_{\text{eff}}} (\cos(\omega_q t) \hat{\sigma}_x - \sin(\omega_q t) \hat{\sigma}_y) - \frac{\Delta}{\Omega_{\text{eff}}} \hat{\sigma}_z \right)} \\
&= e^{-itn\Delta} \begin{pmatrix} \cos\left(\frac{\Omega_{\text{eff}}t}{2}\right) + i \cdot \sin\left(\frac{\Omega_{\text{eff}}t}{2}\right) \frac{\Delta}{\Omega_{\text{eff}}} & -i \cdot \sin\left(\frac{\Omega_{\text{eff}}t}{2}\right) \frac{\Omega\sqrt{n}}{\Omega_{\text{eff}}} e^{i\omega_q t} \\ -i \cdot \sin\left(\frac{\Omega_{\text{eff}}t}{2}\right) \frac{\Omega\sqrt{n}}{\Omega_{\text{eff}}} e^{-i\omega_q t} & \cos\left(\frac{\Omega_{\text{eff}}t}{2}\right) - i \cdot \sin\left(\frac{\Omega_{\text{eff}}t}{2}\right) \frac{\Delta}{\Omega_{\text{eff}}} \end{pmatrix}
\end{aligned} \tag{S28}$$

where we define $\Omega_{\text{eff}} = \sqrt{\Delta^2 + n\Omega^2}$. For free evolution when $\Omega \rightarrow 0$, we get:

$$e^{-i\hat{H}_{\text{int}}t/\hbar} = e^{-itn\Delta} \begin{pmatrix} e^{it\frac{\Delta}{2}} & 0 \\ 0 & e^{-it\frac{\Delta}{2}} \end{pmatrix} = e^{-it\frac{\Delta}{2}} \begin{pmatrix} e^{-it(n-1)\Delta} & 0 \\ 0 & e^{-itn\Delta} \end{pmatrix} \tag{S29}$$

Considering the following bare eigenstates, their free time-evolution becomes:

$$|0, e\rangle \rightarrow 1, \quad |1, e\rangle \rightarrow e^{-it\Delta}, \quad |2, g\rangle \rightarrow e^{-it2\Delta}. \tag{S30}$$

The state evolution with the first qubit and computational resonator right after the MOVE derived from the circuit can now be written as:

$$|0, g\rangle \rightarrow -i |0, e\rangle \rightarrow -|1, g\rangle. \tag{S31}$$

Since -1 is a global phase, we can neglect it. In the following, we use the previously introduced shorthand notation $c_2 = \cos\left(\frac{\sqrt{2}\pi}{2}\right)$ and $s_2 = \sin\left(\frac{\sqrt{2}\pi}{2}\right)$. In the subsequent part of the circuit up to the second MOVE, the second qubit and computational resonator state becomes:

$$\begin{aligned}
|1, g\rangle &\rightarrow \frac{|1, g\rangle - i |1, e\rangle}{\sqrt{2}} \rightarrow \frac{1}{\sqrt{2}} (-i |0, e\rangle - i (c_2 |1, e\rangle - i s_2 |2, g\rangle)) \\
&= \frac{1}{\sqrt{2}} (-i |0, e\rangle - i c_2 |1, e\rangle - s_2 |2, g\rangle) \\
&= \frac{-i}{\sqrt{2}} (|0, e\rangle + c_2 |1, e\rangle - i s_2 |2, g\rangle)
\end{aligned} \tag{S32}$$

In the reference frame, when the qubit and resonator are far detuned and the interaction term is considered to be negligible, we see from Eqs. (S30) that the free time-evolution of the state becomes:

$$e^{-i\hat{H}t/\hbar} |\psi\rangle = \frac{1}{\sqrt{2}} (|0, e\rangle + c_2 |1, e\rangle e^{-it\Delta} - i \cdot s_2 |2, g\rangle e^{-it2\Delta}) \quad (\text{S33})$$

After the second MOVE gate:

$$\frac{1}{\sqrt{2}} \left(-i |1, g\rangle + c_2 (c_2 |1, e\rangle - is_2 |2, g\rangle) e^{-it\Delta} - is_2 (c_2 |2, g\rangle - is_2 |1, e\rangle) e^{-it2\Delta} \right) \quad (\text{S34})$$

$$= \frac{1}{\sqrt{2}} \left(-i |1, g\rangle \right) \quad (\text{S35})$$

$$+ |1, e\rangle ((c_2)^2 e^{-it\Delta} - (s_2)^2 e^{-it2\Delta}) \quad (\text{S36})$$

$$- i |2, g\rangle c_2 s_2 (e^{-it\Delta} + e^{-it2\Delta}) \quad (\text{S37})$$

$$= \frac{i}{\sqrt{2}} \left(|1, g\rangle \right) \quad (\text{S38})$$

$$+ i |1, e\rangle ((c_2)^2 e^{-it\Delta} - (s_2)^2 e^{-it2\Delta}) \quad (\text{S39})$$

$$+ |2, g\rangle c_2 s_2 (e^{-it\Delta} + e^{-it2\Delta}) \quad (\text{S40})$$

$$(\text{S41})$$

After the final $\frac{\pi}{2}$ -pulse we obtain the following state:

$$\frac{1}{2} \left((|1, g\rangle - i |1, e\rangle) \right) \quad (\text{S42})$$

$$+ i(-i |1, g\rangle + |1, e\rangle) ((c_2)^2 e^{-it\Delta} - (s_2)^2 e^{-it2\Delta}) \quad (\text{S43})$$

$$+ (|2, g\rangle - i |2, e\rangle) c_2 s_2 (e^{-it\Delta} + e^{-it2\Delta}) \quad (\text{S44})$$

$$= \frac{1}{2} \left(|1, g\rangle (1 + (c_2)^2 e^{-it\Delta} - (s_2)^2 e^{-it2\Delta}) \right) \quad (\text{S45})$$

$$- i |1, e\rangle (1 - (c_2)^2 e^{-it\Delta} + (s_2)^2 e^{-it2\Delta}) \quad (\text{S46})$$

$$+ |2, g\rangle c_2 s_2 (e^{-it\Delta} + e^{-it2\Delta}) \quad (\text{S47})$$

$$- i |2, e\rangle c_2 s_2 (e^{-it\Delta} + e^{-it2\Delta}) \quad (\text{S48})$$

$$(\text{S49})$$

The final probabilities of the qubit being in the excited state can be written as

$$P_e = \sum_{n=0}^{\infty} |\langle n, e | \psi \rangle|^2 = \langle \psi | 1, e \rangle \langle 1, e | \psi \rangle + \langle \psi | 2, e \rangle \langle 2, e | \psi \rangle. \quad (\text{S50})$$

The last equality follows from the fact that we only consider the first and the second excitation manifold. These terms are

$$\begin{aligned} P_{1e} &= \langle \psi | 1, e \rangle \langle 1, e | \psi \rangle \\ &= \frac{1}{4} (1 - (c_2)^2 e^{it\Delta} + (s_2)^2 e^{it2\Delta}) (1 - (c_2)^2 e^{-it\Delta} + (s_2)^2 e^{-it2\Delta}) \\ &= \frac{1}{4} [1 - 2(c_2)^2 \cos(t\Delta) + 2(s_2)^2 \cos(t2\Delta) - 2(c_2)^2 (s_2)^2 \cos(t\Delta) + (c_2)^4 + (c_2)^4] \end{aligned} \quad (\text{S51})$$

$$P_{2e} = \langle \psi | 2, e \rangle \langle 2, e | \psi \rangle \quad (\text{S52})$$

$$\frac{(c_2 s_2)^2}{4} (e^{it\Delta} + e^{it2\Delta}) (e^{-it\Delta} + e^{-it2\Delta}) \quad (\text{S53})$$

$$= \frac{(c_2 s_2)^2}{2} (1 + \cos(t\Delta)). \quad (\text{S54})$$

$$(\text{S55})$$

Taking the sum of these equations, the full qubit excitation becomes:

$$P_e = \frac{1}{2} (1 - c_2^2 \cos(\Delta t) + s_2^2 \cos(2\Delta t)) \quad (\text{S56})$$

3. Populated Ramsey experiment

We generalize the populated Ramsey experiment to arbitrary resonator states. For simplicity, we assume ideal JC interaction without any additional phase shifts here, the calculation for the imperfect JC interaction is analogous but requires a bit more book keeping. We assume the initial state

$$|\psi\rangle = \sum_n \alpha_n |g, n\rangle. \quad (\text{S57})$$

Applying the first $\pi/2$ -pulse, followed by the first MOVE gate in the Ramsey sequence leads to

$$|\psi\rangle = \frac{1}{\sqrt{2}} \sum_n \alpha_n \left\{ c_n |g, n\rangle - i s_n |e, n-1\rangle - i c_{n+1} |e, n\rangle - s_{n+1} |g, n+1\rangle \right\}. \quad (\text{S58})$$

Subsequent time evolution in the lab frame is

$$|g, n\rangle \rightarrow |g, n\rangle e^{in\omega_r t}, \quad |e, n\rangle \rightarrow |g, n\rangle e^{in\omega_r t + i\omega_q t}. \quad (\text{S59})$$

After the final MOVE gate, the state can be written as

$$|\psi\rangle = \frac{1}{\sqrt{2}} \sum_n \alpha_n \left\{ \beta_n |g, n\rangle + \gamma_n |e, n\rangle + \lambda_n |e, n-1\rangle + \kappa_n |g, n+1\rangle \right\}, \quad (\text{S60})$$

where

$$\beta_n \equiv c_n^2 e^{in\omega_r t} - s_n^2 e^{i(n-1)\omega_r t + i\omega_q t}, \quad \gamma_n \equiv -i \left[c_{n+1}^2 e^{in\omega_r t + i\omega_q} - s_{n+1}^2 e^{i(n+1)\omega_r t} \right] \quad (\text{S61})$$

$$\lambda_n \equiv -i c_n s_n \left[e^{i(n-1)\omega_r t + i\omega_q t} + e^{in\omega_r t} \right], \quad \kappa_n \equiv -c_{n+1} s_{n+1} \left[e^{in\omega_r t + i\omega_q t} + e^{i(n+1)\omega_r t} \right]. \quad (\text{S62})$$

The final state can be formally expressed as

$$|\psi\rangle = \frac{1}{2} \sum_n \alpha_n \left\{ (\gamma_n - i\beta_n) |e, n\rangle + \lambda_n |e, n-1\rangle + \kappa_n |e, n+1\rangle \right\} + |g\rangle \text{ contribution}. \quad (\text{S63})$$

Thus, the excited state probability is

$$P_e = \frac{1}{4} \sum_n |\alpha_n|^2 \left\{ |\gamma_n - i\beta_n|^2 + |\lambda_n|^2 + |\kappa_n|^2 \right\}. \quad (\text{S64})$$

The individual probabilities can be expressed as

$$|\gamma_n - i\beta_n|^2 = c_n^4 + s_n^4 + c_{n+1}^4 + s_{n+1}^4 - 2c_{n+1}^2 s_{n+1}^2 \cos((\omega_r - \omega_r)t) \quad (\text{S65})$$

$$+ 2c_n^2 c_{n+1}^2 \cos(\omega_q t) - 2c_{n+1}^2 s_n^2 \cos(\omega_r t) - 2c_n^2 s_{n+1}^2 \cos(\omega_r t) \quad (\text{S66})$$

$$- 2s_s^2 s_{n+1}^2 \cos((2\omega_r - \omega_q)t) - 2c_n^2 s_n^2 \cos((\omega_r - \omega_q)t), \quad (\text{S67})$$

$$|\lambda_n|^2 \equiv 2c_n^2 s_n^2 [1 + \cos((\omega_r - \omega_q)t)], \quad |\kappa_n|^2 \equiv 2c_{n+1}^2 s_{n+1}^2 [1 + \cos((\omega_r - \omega_q)t)]. \quad (\text{S68})$$

Note that just as for the two-photon case, there are only second harmonic contributions $2\omega_r$ from the resonator. The reason is the equidistant spacing of the harmonic oscillator combined with the 2×2 matrix block structure of the JC Hamiltonian, implying that all rotating contributions spaced apart further than $2\omega_r$ act as a global phase for the respective state probabilities and thus drop out. The final result in the lab frame is given by

$$P_e = \frac{1}{2} \sum_n |\alpha_n|^2 \left\{ 1 + c_n^2 s_n^2 \cos(\omega_q t) - (c_{n+1}^2 s_n^2 + c_n^2 s_{n+1}^2) \cos(\omega_r t) + s_n^2 s_{n+1}^2 \cos((2\omega_r - \omega_q)t) \right\} \quad (\text{S69})$$

And the detected probability (assuming virtual detuning $\Omega = 0$) is

$$P_e = \frac{1}{2} \sum_n |\alpha_n|^2 \left\{ 1 + c_n^2 s_n^2 - (c_{n+1}^2 s_n^2 + c_n^2 s_{n+1}^2) \cos(\Delta t) + s_n^2 s_{n+1}^2 \cos(2\Delta t) \right\}. \quad (\text{S70})$$

In the case $n = 0$, this expression reproduces the standard Ramsey oscillations and for $n = 1$, we reproduce Eq. (6) without any phase shifts.

4. Phase correction via modified Resonator T2 Ramsey experiment

In this section, we derive Eq. (6), describing the non-ideal populated resonator Ramsey experiment. In a realistic experimental setting, the JC interaction is not ideal, but of the form of a general excitation-preserving exchange (“fSim”). To use the JC gate for actual algorithm applications, the phases $(\gamma_n, \chi_n, \zeta_n)$ need to be calibrated for each JC block. In the single-photon manifold, where only the phase γ needs to be calibrated since MOVE is only applied pair-wise and the resonator state is never directly read out, this is done via a VZ rotation. We assume that this VZ calibration for the MOVE gate is ideal ($\gamma_1 = 0$). The populated Ramsey experiment can then be used to calibrate the phases for the two-photon manifold. The state after the second MOVE gate in the populated resonator Ramsey sequence can be expressed as

$$|\psi\rangle \rightarrow |\psi\rangle = \frac{i}{\sqrt{2}} (|1, g\rangle e^{i\omega_q t} + a|1, e\rangle + b|2, g\rangle), \quad (\text{S71})$$

where we have

$$a \equiv i \left(c_+^2 e^{i(\omega_q + \omega_r)t} - s_- s_+ e^{2i\omega_r t} \right), \quad b \equiv c_+ s_- e^{i(\omega_q + \omega_r)t} + c_- s_- e^{2i\omega_r t}, \quad (\text{S72})$$

with the abbreviation $c_{\pm}, s_{\pm} \equiv c_2^{\pm}, s_2^{\pm}$ [cf. Eq. (5)]. In this case, we find

$$P_{1e} = \frac{1}{4} [1 + c_2^4 + s_2^4 - 2c_2^2 \cos(\omega_r t - 2\gamma_2 - 2\zeta_2) + 2s_2^2 \cos(2\omega_r t - \omega_q t - 2\gamma_2) - 2c_2^2 s_2^2 \cos(\omega_r t - \omega_q t + 2\zeta_2)] \quad (\text{S73})$$

$$P_{2e} = \frac{c_2^2 s_2^2}{2} [1 + \cos((\omega_r - \omega_q)t + 2\zeta_2)]. \quad (\text{S74})$$

Also in this case, the Ramsey sequence filters the terms rotating with frequency $\omega_r - \omega_q$. The detected excited state probability in the qubit rotating frame is

$$P_e = \frac{1}{2} [1 - c_2^2 \cos(\Delta t - 2\gamma_2 - 2\zeta_2) + s_2^2 \cos(2\Delta t - 2\gamma_2)], \quad (\text{S75})$$

i.e., the non-calibrated phases in the JC interaction directly manifest as phase shifts of the detected populated Ramsey interference pattern. To restore the ideal interference pattern, one can compensate for these phase shifts by introducing additional control degrees of freedom. Since the relative phase χ is not relevant in Eq. S79 (no swap between different qubits), two degrees of freedom are required. In the simplest case, those can be just included in the form of subsequent physical z-rotations with phases φ and φ' after each MOVE gate in the Ramsey sequence.

For this modified circuit, the state after the first MOVE gate in the Ramsey sequence transforms to

$$|\psi\rangle \rightarrow |\psi\rangle = -\frac{1}{\sqrt{2}} (|0, e\rangle e^{i\varphi} + c_+ |1, e\rangle e^{i\varphi} - i s_- |2, g\rangle), \quad (\text{S76})$$

and after the second MOVE gate

$$|\psi\rangle \rightarrow |\psi\rangle = \frac{i}{\sqrt{2}} (|1, g\rangle e^{i\omega_q t + i\varphi} + a|1, e\rangle + b|2, g\rangle), \quad (\text{S77})$$

where we have to redefine a and b as

$$a \equiv i \left(c_+^2 e^{i(\omega_q + \omega_r)t + i\varphi'} - s_- s_+ e^{2i\omega_r t + i(\varphi - \varphi')} \right), \quad b \equiv c_+ s_- e^{i(\omega_q + \omega_r)t + i\varphi} + c_- s_- e^{2i\omega_r t}. \quad (\text{S78})$$

The final result, obtained in complete analogy to the previous calculations, is given by

$$P_e = \frac{1}{2} [1 - c_2^2 \cos(\Delta t - 2\gamma_2 - 2\zeta_2 + \varphi') + s_2^2 \cos(2\Delta t - 2\gamma_2 + \varphi' - \varphi)]. \quad (\text{S79})$$

It is then predicted that the ideally expected result can be restored by employing the control relations

$$\varphi = 2\zeta_2, \quad \varphi' = 2\gamma_2 + 2\zeta_2. \quad (\text{S80})$$